

## Nocturnal Turbulence at Jezero Crater as Determined From MEDA Measurements and Modeling



### Special Section:

The Mars Perseverance Rover  
Jezero Crater Floor Campaign

### Key Points:

- Nocturnal turbulence at Jezero crater peaks at  $L_s \sim 37$ ,  $L_s \sim 56$ , and  $L_s \sim 123$  with a clear hiatus lasting tens of sols centered at  $L_s \sim 83$
- Both observations and modeling show turbulence during the first part of the night and around midnight
- Turbulence is produced by wind shear originating from the passage of an atmospheric bore wave related to downslope winds from the west rim

### Supporting Information:

Supporting Information may be found in the online version of this article.

### Correspondence to:















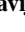


J. Pla-García,  
[jpla@cab.inta-csic.es](mailto:jpla@cab.inta-csic.es)

### Citation:

Pla-García, J., Manguira, A., Rafkin, S., Newman, C., Bertrand, T., Martínez, G., et al. (2023). Nocturnal turbulence at Jezero crater as determined from MEDA measurements and modeling. *Journal of Geophysical Research: Planets*, 128, e2022JE007607. <https://doi.org/10.1029/2022JE007607>

Received 4 OCT 2022

Accepted 7 JUL 2023

Jorge Pla-García<sup>1</sup> , A. Manguira<sup>2</sup> , S. Rafkin<sup>3</sup>, C. Newman<sup>4</sup> , T. Bertrand<sup>5</sup> , G. Martínez<sup>6</sup> , R. Hueso<sup>2</sup> , A. Sánchez-Lavega<sup>2</sup> , T. del Río Gaztelurrutia<sup>2</sup> , A. Stott<sup>7</sup> , N. Murdoch<sup>7</sup> , M. de la Torre Juárez<sup>8</sup> , M. Lemmon<sup>9</sup> , B. Chide<sup>10</sup> , D. Viúdez-Moreiras<sup>1</sup> , H. Savijarvi<sup>11</sup> , M. Richardson<sup>4</sup>, M. Marín<sup>1</sup>, E. Sebastian<sup>1</sup>, A. Lepinette-Malvitte<sup>1</sup> , L. Mora<sup>1</sup> , and J. A. Rodríguez-Manfredi<sup>1</sup>

<sup>1</sup>Centro de Astrobiología (CAB), CSIC-INTA, Madrid, Spain, <sup>2</sup>Universidad del País Vasco (UPV/EHU), Bilbao, Spain, <sup>3</sup>Southwest Research Institute, Boulder, CO, USA, <sup>4</sup>Aeolis Research, Chandler, AZ, USA, <sup>5</sup>LESIA, Observatoire de Paris, Paris, France, <sup>6</sup>Lunar and Planetary Institute, Houston, TX, USA, <sup>7</sup>Institut Supérieur de l'Aéronautique et de l'Espace (ISAE-SUPAERO), Université de Toulouse, Toulouse, France, <sup>8</sup>Jet Propulsion Laboratory, California Institute of Technology, Pasadena, CA, USA, <sup>9</sup>Space Science Institute, Boulder, CO, USA, <sup>10</sup>Space and Planetary Exploration Team, Los Alamos National Laboratory, Los Alamos, NM, USA, <sup>11</sup>Finnish Meteorological Institute, Helsinki, Finland

**Abstract** Mars 2020 Mars Environmental Dynamics Analyzer (MEDA) instrument data acquired during half of a Martian year ( $L_s$  13°–180°), and modeling efforts with the Mars Regional Atmospheric Modeling System (MRAMS) and the Mars Climate Database (MCD) enable the study of the seasonal evolution and variability of nocturnal atmospheric turbulence at Jezero crater. Nighttime conditions in Mars's Planetary Boundary Layer are highly stable because of strong radiative cooling that efficiently inhibits convection. However, MEDA nighttime observations of simultaneous rapid fluctuations in horizontal wind speed and air temperatures suggest the development of nighttime turbulence in Jezero crater. Mesoscale modeling with MRAMS also shows a similar pattern and enables us to investigate the origins of this turbulence and the mechanisms at play. As opposed to Gale crater, less evidence of turbulence from breaking mountain wave activity was found in Jezero during the period studied with MRAMS. On the contrary, the model suggests that nighttime turbulence at Jezero crater is explained by increasingly strong wind shear produced by the development of an atmospheric bore-like disturbance at the nocturnal inversion interface. These atmospheric bores are produced by downslope winds from the west rim undercutting a strong low-level jet aloft from ~19:00 to 01:00 LTST and from ~01:00 LTST to dawn when undercutting weak winds aloft. The enhanced wind shear leads to a reduction in the Richardson number and an onset of mechanical turbulence. Once the critical Richardson Number is reached ( $Ri \sim <0.25$ ), shear instabilities can mix warmer air aloft down to the surface.

**Plain Language Summary** Mars is highly susceptible to atmospheric turbulence, which refers to the chaotic and instantaneous variation in the thermodynamic magnitudes of the atmosphere. While the Martian nighttime conditions near the surface are typically stable due to strong radiative cooling that efficiently inhibits convection, turbulence can still occur due to wind shear. Wind shear is defined as a change in wind speed and/or direction over a relatively short distance in the atmosphere. This phenomenon can mechanically force turbulence as described in this study using both Mars 2020 rover observations at Jezero crater and numerical modeling efforts. Both observations and modeling show turbulence during the first part of the night and around midnight during most of the times of the year with a clear hiatus in turbulence centered prior to summer solstice. We provide evidence that points toward the wind shear turbulence being caused by atmospheric bore waves inside the crater.

## 1. Introduction

The Mars 2020 Perseverance rover landed on Mars in February 2021, corresponding to a solar longitude ( $L_s$ ) of ~5° in the Martian Year (MY) 36, at 18.44°N; 77.45°E within and near the west rim of Jezero crater, a ~45 km diameter impact crater located in the northwest rim of the Isidis Basin close to the Nili Fossae region of Mars (Figure 1).

The aim of this article is to explore the nocturnal and seasonal variability of atmospheric turbulence monitored by the Mars 2020 mission over half of the Martian year MY36, from mission sol 15 corresponding to Mars

© 2023. The Authors.

This is an open access article under the terms of the [Creative Commons Attribution License](https://creativecommons.org/licenses/by/4.0/), which permits use, distribution and reproduction in any medium, provided the original work is properly cited.

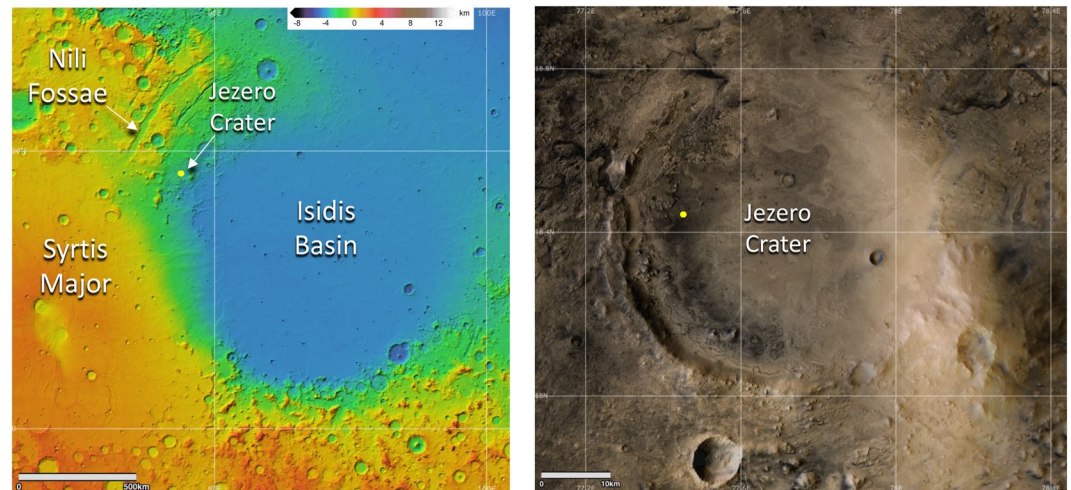


**Figure 1.** (left) Jezero crater sits inside and close to the NW rim of the huge Isidis Basin, shown as color-coded elevation (m) from the Mars Orbiter Laser Altimeter (MOLA). (right) Jezero crater view from the Context Camera (CTX) onboard the Mars Reconnaissance Orbiter. The yellow dot represents the Mars 2020 Perseverance rover landing site location.

areocentric solar orbital longitude  $L_s \sim 13^\circ$  (in early northern spring) up to sol 361 corresponding to  $L_s \sim 180^\circ$  (northern fall equinox). Turbulent kinetic energy (hereafter TKE), which measures turbulence intensity in a flow in the planetary boundary layer (hereafter PBL) arises from two sources: buoyancy and wind shear (Stull, 1988). During Martian nights, near-surface temperature inversions act as a buoyancy sink that suppresses turbulence (Munguira et al., 2023; Read et al., 2017). Therefore, wind shear becomes the primary source of local turbulence. According to Chatain et al. (2021), nighttime turbulence at the InSight landing site situated at Elysium Planitia ( $4.5^\circ\text{N } 135.6^\circ\text{E}$ ) is produced by wind shear and is almost as strong as daytime convective-driven turbulence around perihelion ( $L_s \sim 251^\circ$ ) due to the combination of a low-level jet (associated with strong ambient wind) and weak stability. A low-level jet (hereafter LLJ) refers to a narrow, fast-moving air stream in the lower atmosphere (Davis, 2000; Thorpe & Guymmer, 1977) and the formation on Mars is influenced by various factors such as topography, thermal effects, etc (Joshi et al., 1997). Rafkin et al. (2016) also noted nocturnal turbulence at Gale crater throughout all seasons, as evidenced by fast temperature fluctuations, with the strongest perturbations occurring at  $L_s 270^\circ$ , when northern crater rims initiate large amplitude strong breaking mountain waves that force warmer air masses to descend and reach the crater floor.

Prior to Mars 2020's landing, Pla-García et al. (2020) performed high-resolution meteorological simulations of Jezero crater at  $L_s 0^\circ, 90^\circ, 180^\circ$ , and  $270^\circ$  and predicted strong nocturnal turbulence, especially at  $L_s \sim 180^\circ$ . In this study, we report observations of nocturnal turbulence made by Mars 2020's Mars Environmental Dynamics Analyzer (MEDA) that confirm these pre-landing predictions and use our original Mars Regional Atmospheric Modeling System (hereafter MRAMS; Rafkin et al., 2001, 2002; Rafkin, 2009; Rafkin & Michaels, 2019) simulations and additional ones at other  $L_s$  to interpret key periods observed in the first half of the MY. MRAMS has previously demonstrated the ability to reproduce the observed meteorological conditions on Mars (Pla-García et al., 2016, 2019). Because running MRAMS for an entire Mars year is not feasible, the model was run for six solar longitudes every  $30^\circ$ :  $L_s \sim 30^\circ, 60^\circ, 90^\circ, 120^\circ, 150^\circ$ , and  $180^\circ$ , corresponding to Mars 2020 mission sols  $\sim 50, 116, 182, 247, 307$ , and  $361$ , respectively. All times shown in observations and simulations are in Local True Solar Time (hereafter LTST). We define the nocturnal period as the time between 19:00 and 05:00 LTST because the sun sets between 18:00 ( $L_s \sim 180^\circ$ ) and 18:36 LTST ( $L_s \sim 90^\circ$ ) and rises between 05:25 ( $L_s \sim 90^\circ$ ) and 06:00 LTST ( $L_s \sim 180^\circ$ ).

MRAMS diurnal cycle results shown in Section 2 are in good agreement with MEDA observations, and this agreement provides justification for utilizing the model results to investigate the nocturnal turbulence environment of the Jezero crater region. We have also used Mars Climate Database (hereafter MCD, Lewis et al., 1999; Millour et al., 2022) results to provide a global context for the MRAMS regional and local scale predictions.

The structure of the article is as follows: Section 2 shows the methodology used in this study, including a description of the MEDA instrument (Section 2.1), a description of the method to compute the MEDA horizontal TKE and the criteria followed to interpret events of atmospheric turbulence (Section 2.2), a brief description

of MRAMS model configuration (Section 2.3), the comparison of the MRAMS model predictions with MEDA data for the relevant meteorological variables (Section 2.4) and a brief description of MCD model configuration (Section 2.5). Section 3 shows the results and is also divided into 6 subsections devoted to MEDA horizontal TKE (Section 3.1), MRAMS TKE (Section 3.2), the correlation between MEDA horizontal TKE and MEDA temperature oscillations (Section 3.3), Richardson number (Section 3.4), MRAMS vertical profiles (Section 3.5) and the contributions of the large-scale to Jezero crater turbulence using MCD (Section 3.6). Section 4 contains the Summary and Conclusions.

## 2. Methods

Here, we explain MEDA observations with a focus on Wind Sensors (WS), the Air Temperature Sensors (ATS) and the Thermal Infrared Sensor (TIRS) (Section 2.1) and a description of the method to compute the horizontal TKE with MEDA and the criteria followed to interpret events of atmospheric turbulence (Section 2.2). Furthermore, we include a brief description of the MRAMS model configuration used (Section 2.3), a MRAMS model comparison with MEDA data for validation (Section 2.4) and a brief description of the MCD model configuration used in the study (Section 2.5).

### 2.1. The MEDA Instrument

The MEDA sensor suite (Newman et al., 2022; Rodríguez-Manfredi et al., 2021) data used in this analysis of nighttime atmospheric turbulence are provided by the WS, ATS and TIRS. Both WS and ATS can be operated with a measurement frequency up to 2 Hz, whereas TIRS is limited to a frequency of 1 Hz. MEDA acquires data typically over 50% of a full sol, measuring at odd hours during odd sols and even hours during even sols, so the combination of data from consecutive sols allows the study of timescales ranging from seconds to diurnal cycles and their seasonal evolution.

Wind data are taken by two WSs on two booms located around the rover's Remote Sensing Mast (hereafter RSM) at  $\sim 1.5$  m height above the ground, separated  $\sim 120^\circ$  from each other in the horizontal plane. Two are needed to correct for the effects of thermal and mechanical interference by rover hardware, which disrupts winds approaching from different directions depending on the boom (Rodríguez-Manfredi et al., 2021). Measurements from both WS are compared and the boom least affected by rover hardware is identified and used to produce horizontal wind speed and direction values with an accuracy better than  $\pm 1$  m/s and  $\pm 15^\circ$ , and a resolution of 0.5 m/s for wind speeds between 0 and 10 m/s, and 10% accuracy and 1 m/s resolution for wind speeds above 10 up to 40 m/s (Rodríguez-Manfredi et al., 2021). The MEDA WS can also potentially characterize the vertical component of the wind for the first time, but no vertical winds are currently available, although ongoing calibration efforts are aimed at retrieving those values. For this reason, we are computing the MEDA TKE using only horizontal winds at 1.5 m height (see Section 2.2). Only horizontal wind data from sols 15 to 313 ( $L_s \sim 152^\circ$ ) are included in this study because on sols 313 and 315 several boards of the WS were damaged due to wind-induced grain impacts (Hueso et al., 2022), thus preventing high-accuracy wind retrievals since that time.

TIRS is the first in situ Martian IR radiometer that includes upward- and downward-looking channels (Pérez-Izquierdo et al., 2018; Rodríguez-Manfredi et al., 2021; Sebastián et al., 2020, 2021). The TIRS air temperature from an atmospheric layer with peak emission at 40 m used in this analysis of nighttime atmospheric turbulence is provided by the IR2 flux channel (Smith et al., 2006) and the TIRS surface brightness temperature data used for the calculation of the MEDA bulk Richardson number are provided by the IR5 flux channel.

Air temperatures were measured by MEDA using five thermocouple sensors. Three of them (ATS1, ATS2, and ATS3) are located on the RSM at 1.45 m above the ground, separated azimuthally  $\sim 120^\circ$  from each other in the horizontal plane to ensure that at least one is always upwind from the RSM and hence the environmental winds can couple this sensor with the atmosphere (Munguira et al., 2023). Two others (ATS4 and ATS5) are attached to the sides of the rover at a height of 0.84 m. All ATS have accuracy and resolution better than 1 and 0.1 K, respectively (Rodríguez-Manfredi et al., 2021). ATS1, ATS2, and ATS3 typically provide similar values and are less affected by the thermal influence of the rover compared to ATS4 and ATS5, which are closer to the rover body and less exposed to winds (Munguira et al., 2023). Thermal plumes generated by the Radioisotope Thermoelectric Generator (hereafter RTG) can have an impact on air temperature measurements when the wind blows from the direction of the RTG toward the sensors (ATS1, ATS2, and ATS3) with a speed that falls between certain threshold values, typically ranging between 2 and 4 m/s according to Lorenz and Sotzen (2014).

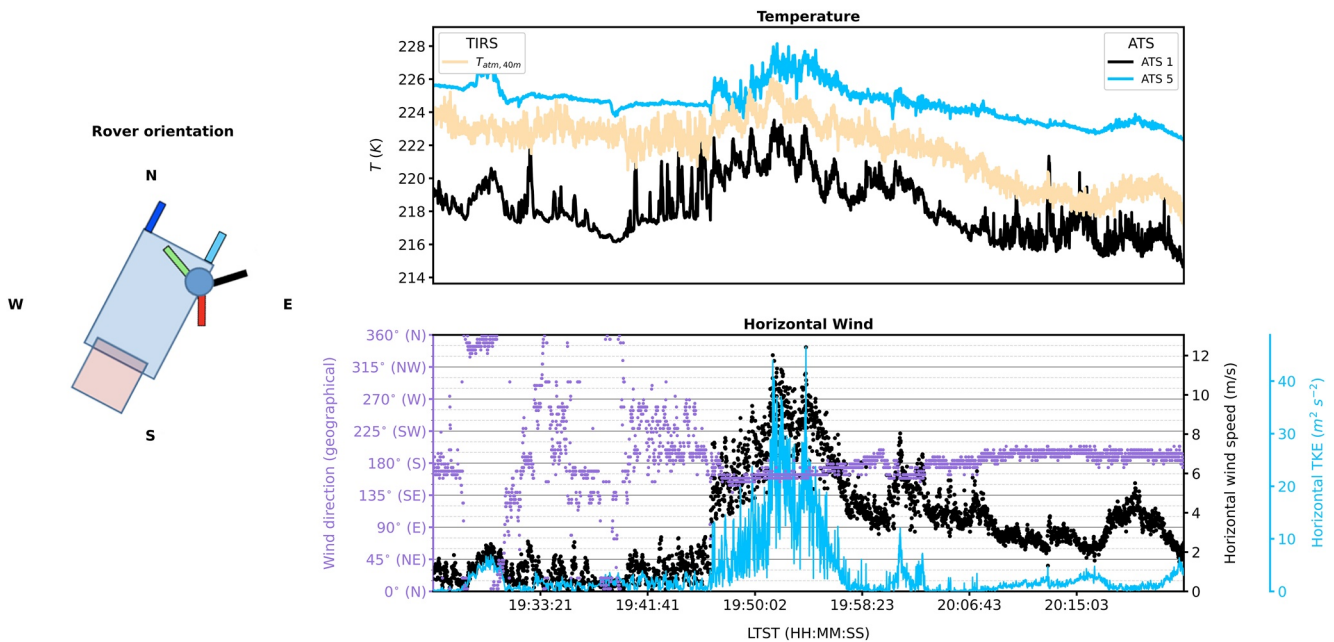


**Figure 2.** (left) The rover orientation for this period and placement of the five Air Temperature Sensors (ATS1 and ATS5 colored as in the upper right-hand plot), to aid in analyzing thermal contamination from the rover's RTG and deck. (right) MEDA data from 19:25 through 20:25 on sol 213 ( $L_s$  104), showing (top) 0.85 m ATS5 air temperatures (light blue line), 1.45 m ATS1 air temperatures (black line), and ~40 m air temperature (cream line), and (bottom) wind direction (purple dots), wind speed (black dots) and  $TKE_H$  (light blue line, derived from MEDA wind speeds as shown in the text) fluctuations.

## 2.2. The Study of Nighttime Turbulence With MEDA

The TKE is a measure of the turbulence intensity in the PBL. Data from the MEDA WS is used to derive the horizontal components of the TKE, referred to as horizontal TKE (hereafter  $TKE_H$ ):

$$TKE_H = \frac{1}{2} \left( \overline{(u')^2} + \overline{(v')^2} \right), \quad (1)$$

where  $u$  is the zonal component of the wind and  $v$  is the meridional component of the wind that are decomposed into a time average and a fluctuating term:  $u = \bar{u} + u'$ . MEDA wind data are divided into 5-min windows, where  $\bar{u}$  is accounted for by a polynomial fit of degree 2 to separate small-scale fluctuations from longer period variations such as the diurnal evolution. Hence, the time series of the fluctuating terms in Equation 1,  $u'$  and  $v'$ , are retrieved by subtracting these polynomial fits from  $u$  and  $v$ . Making use of Equation 1, we get  $TKE_H$  values every 5 min. Occasionally, for a closer comparison with temperatures, we calculate  $TKE_H$  at 1 Hz (Figures 2 and 7; Figures S1–S6 in Supporting Information S1) instead of retrieving the average  $TKE_H$ , for which we introduce the first and second terms on the right side of Equation 1 as two (squared) time series, without averaging them. The lack of the vertical component of the wind in MEDA measurements implies that the total TKE cannot be quantified from observations. Even so, MEDA  $TKE_H$  is a reasonable proxy for TKE because during nighttime stable conditions with mechanical turbulence, we expect the partitioning of TKE to favor  $TKE_H$  as opposed to daytime buoyancy-driven turbulence, especially near the ground where vertical wind speed is constrained ( $w \sim 0$ ) due to boundary conditions. Our analysis of MEDA  $TKE_H$  is supported by model simulations and MEDA temperature data.

ATS and TIRS data were used in conjunction with  $TKE_H$  to investigate the correlation of temperature changes at the times of increased  $TKE_H$ . Simultaneous large values of  $TKE_H$  and positive temperature fluctuations support the hypothesis of shear-driven mixing of air in the stable nighttime atmosphere. ATS1, ATS5, and TIRS share similar orientations (Munguira et al., 2023), and an unambiguous observation of a turbulent mixing event requires the data from the three sensors to be in accordance.

Of the three ATS on the RSM, ATS1 is used in this study as it is the sensor least likely to experience mechanical contamination from the rover. This is because it is pointed  $50^\circ$  clockwise from the rover chassis  $X$  axis (Perez-Grande et al., 2017) and hence has the most approach directions from which the wind does not pass over or around the rover elements to reach it. By contrast, ATS2 and ATS3 both point toward—or over—more of the

**Table 1**

*Modeled Seasons and Corresponding MSL Operational Sols*

Modeled seasons and corresponding mars 2020 operational sols	
$L_s$	Operational Sol
30	50
60	116
90	182
120	247
150	307
180	361

rover hardware. Likewise, ATS5 is relevant in this study because it is least likely to be thermally contaminated by RTG plumes due to its location at the front right of the rover body. The TIRS FOV is to the front right of the rover, putting it closest to ATS1 and ATS5 in terms of orientation. Therefore, positive temperature fluctuations on ATS1 without a counterpart on ATS5 and TIRS would be ambiguous and disregarded as a turbulent event. With this procedure we may miss some real atmospheric turbulence at the times when winds are unfavorable, but in turn it allows us to be confident in the positive identification of a turbulent event.

Figure 2 shows a time series of atmospheric temperatures at the three height levels, along with simultaneous wind speed, wind directions and  $TKE_H$ . To help illustrate the origin of different temperature peaks, the rover and ATS orientations are shown on the left for context. MEDA data of sol 213 ( $L_s \sim 104^\circ$ ) between 19:25 and 20:25 are displayed to illustrate atmospheric

turbulence as well as thermal contamination from the rover. We identify a turbulent event between  $\sim 19:46$  and  $19:56$  when the  $TKE_H$  and the air temperature at the three heights present positive fluctuations. In addition, the wind was blowing from the S-SE at this time, without passing through the RTG or the rover's deck. Interestingly, peaks in  $TKE_H$  and temperature coincided, both for 10-min long peaks and for higher frequency peaks. It is also significant that the wind speed was remarkably high for this LTST compared to the same time in other sols (Viúdez-Moreiras et al., 2022).

There are other times when ATS1 temperatures increase in Figure 2, but these artificially generated temperature fluctuations do not coincide with peaks in atmospheric temperatures at other altitudes (0.84 and 40 m for ATS5 and TIRS respectively) nor in MEDA  $TKE_H$ . In those cases, ATS1 measurements are compromised by the relative orientation of the rover with respect to the wind direction. For example, between  $\sim 19:40$  and  $\sim 19:46$  the wind blew from SW on average, thus air reached ATS1 after passing over the RTG and the rover deck. At 20:15 the wind is from the SSW, enough to have ATS1 affected by the RTG. And at  $\sim 19:32$  the wind is from a whole range of directions, including SW, enough to cause the ATS1 peak but not peaks at other altitudes. The example in Figure 2 shows that environmental turbulence and artificially generated thermal fluctuations can be distinguished by comparison with the wind data set (Davy et al., 2010; Munguira et al., 2023).

It is important to note that not all the natural temperature fluctuations are related to turbulence, as winds bringing air masses with different temperatures could also produce temperature fluctuations. For this reason, simultaneous winds, and especially  $TKE_H$ , are key to interpret temperatures. Also, because  $TKE_H$  does not include vertical wind speed, it is possible that some nocturnal temperature fluctuations occur due to turbulence caused by vertical air movements that we are unable to detect. In general, the temperature data set is complex, with multiple effects taking part. For this reason, we consider  $TKE_H$  as the best proxy of the nighttime turbulence intensity that MEDA can provide.

### 2.3. MRAMS Mesoscale Model

The MRAMS model is described in detail in Rafkin and Michaels (2019) and was configured for this study with initialization and physics options similar to Pla-García et al. (2020) using seven nested grids with the innermost grids centered on the location of the Mars 2020 Perseverance rover landing site within Jezero crater (Figure 1 of Pla-García et al., 2020). We chose to use the data from the innermost and highest spatial resolution ( $\sim 0.33$  km between points in the horizontal) grid #7. To obtain representative nighttime turbulent conditions to compare with MEDA data, we ran the model for six solar longitudes, corresponding to the particular operational sols for the Mars 2020 Perseverance rover, as indicated in Table 1. These MRAMS data, as well as the programs required to plot them, are provided for the periods studied in this manuscript in Pla-García and Rafkin (2023).

### 2.4. MRAMS Model Comparison With MEDA Data for Validation

Air temperatures and wind speed and direction data obtained from MRAMS are compared with data observed by MEDA. The investigation focuses on a full diurnal cycle at six different times of year ( $L_s$  30°, 60°, 90°, 120°, 150°, and 180°) at the rover location within Jezero crater. The results are presented in Figures 3 and 4. The lowest atmospheric level of the model is situated at  $\sim 14.5$  m above the ground. In theory, the first vertical level would be best placed at the same height as the MEDA sensors ( $\sim 1.5$  m). However, this is not a feasible computational

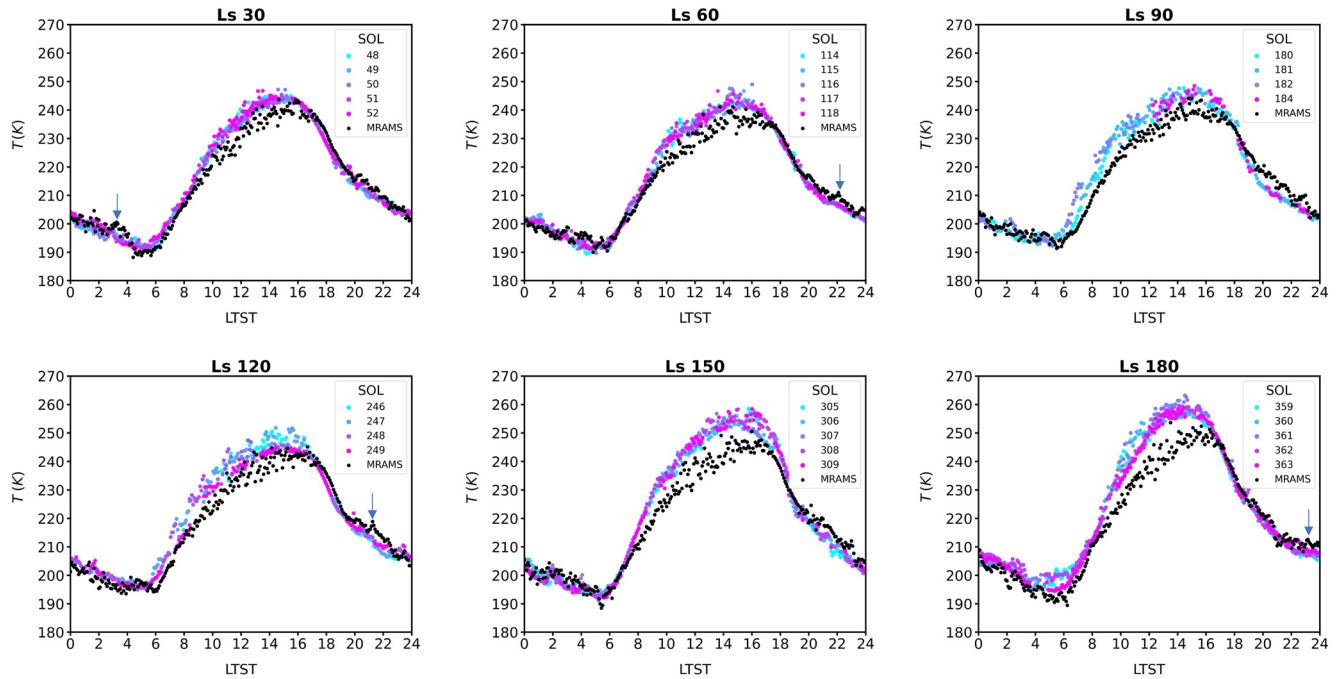


**Figure 3.** MEDA air temperature at  $\sim 1.45$  m measured by the ATS1 within five sols of the given  $L_s$  (colored dots) and Mars Regional Atmospheric Modeling System (MRAMS) data taken from the lowest model level at  $\sim 14.5$  m (black dots). Blue arrows represent examples of times when the model predicts thermal perturbations at the same times as the increases of TKE shown in Figure 6.

option as the integration time step for non-hydrostatic models is closely tied to the thickness of the layer in question. Adopting a minimum model thickness of  $\sim 1.5$  m would necessitate a mother domain time step of mere fractions of a second. As a result, the model simulations would require roughly two orders of magnitude more time to complete (Pla-García et al., 2016).

MRAMS versus MEDA air temperature comparisons are shown in Figure 3. Because the model output comes from  $\sim 13$  m higher above the surface than ATS1 measures, we expect the MRAMS values at higher elevations tend to be cooler than observations in the morning and early afternoon with this difference increasing over the day, and then tend to be warmer in the late afternoon and through the night. This is a direct result of the steep afternoon superadiabatic lapse rate and a strong nocturnal inversion (Schofield et al., 1997; Smith et al., 2004). During the day, the air temperature variations shown in the model and observations can be attributed to convective motions. The sudden increase in air temperature during the evenings at the onset of radiative cooling and the rapid air temperature fluctuations modeled at night across all times of the year (Figure 3) are indicative of nocturnal turbulence that could be mechanically driven (forcing warm air to descend or cold air to rise) since the atmosphere is stable in the evening and at night.

In Figure 4, MRAMS and MEDA generally compare favorably in the wind direction, but some significant differences can arise when MEDA wind speeds are much lower than those obtained from MRAMS (typically  $< 2$  m/s from 01:00 LTST to dawn). During this time of low wind speeds, the MEDA wind directions may not be reliable, as evidenced by the calibration tests conducted using the identical performance APSS-TWINS sensor onboard the InSight lander (Banfield et al., 2020). It is also important to note that winds in the model are obtained from the lowest level at  $\sim 14.5$  m, whereas MEDA data are from an altitude of  $\sim 1.5$  m above the surface. The small difference in height should not have a large impact on the wind direction but can contribute to wind speed differences. Wind speeds at  $\sim 14.5$  m may be faster than at  $\sim 1.5$  m due to frictional effects with the surface. Assuming a simple neutral stability log wind profile (Oken, 1987), a 32% decrease in the wind speed from  $\sim 1.5$  to  $\sim 14.5$  m is expected. Even with this 0.68 correction factor applied, MRAMS wind speeds are still higher than those observed with MEDA between 23:00 and dawn (Figure 4). One possible explanation for this could be that MRAMS modeled downslope winds penetrate too far into the crater during this time of sol (atmospheric circulation animations included in Pla-García et al. (2020) SM consistent with the MRAMS wind direction of Figure 4) compared with other high-resolution model predictions (Newman et al., 2021). Also, MRAMS data are not a point measurement. It is a Reynolds averaged value of the grid, which is very different from the wind speed

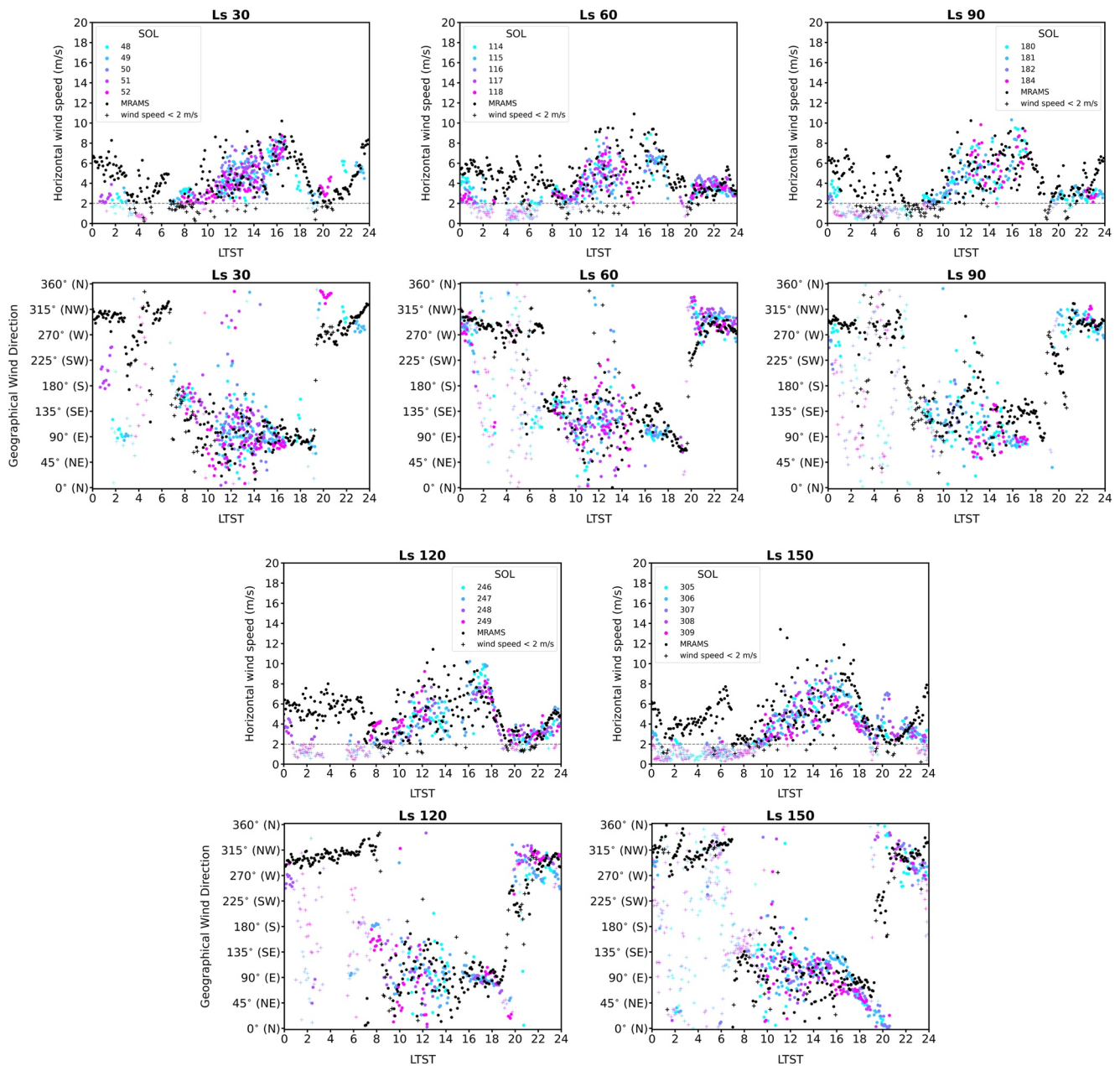


**Figure 4.** Same as Figure 3, but for wind directions and speeds. Note that the MEDA Wind Sensors stopped working after sol 313, so we only have MEDA wind data to compare with  $L_s \sim 30^\circ, 60^\circ, 90^\circ, 120^\circ, 150^\circ,$  and  $180^\circ$ . When wind speeds are lower than 2 m/s (below the dashed line), results (both speeds and directions) are plotted with crosses.

at a single point in space and time. For MRAMS to produce something close to zero, that would mean that every location within the grid is effectively calm. Other contributions that could contribute to the wind speed differences include uncertainties in surface roughness, pressure gradient, errors in the model and/or observational data.

It is also noticeable that the wind speeds are systematically extremely low  $\sim 2$  hr after sunset in MRAMS and MEDA following the collapse of daytime convective PBL (Banfield et al., 2020). At  $\sim 19:30\text{--}20:00$  LTST, the wind speeds start to increase again both in modeling and observations.

Although there are some periods with differences, generally there is a reasonable agreement between MRAMS results and MEDA observations, and this agreement provides justification for utilizing the model results to further investigate the nocturnal turbulence environment of the Jezero crater region.

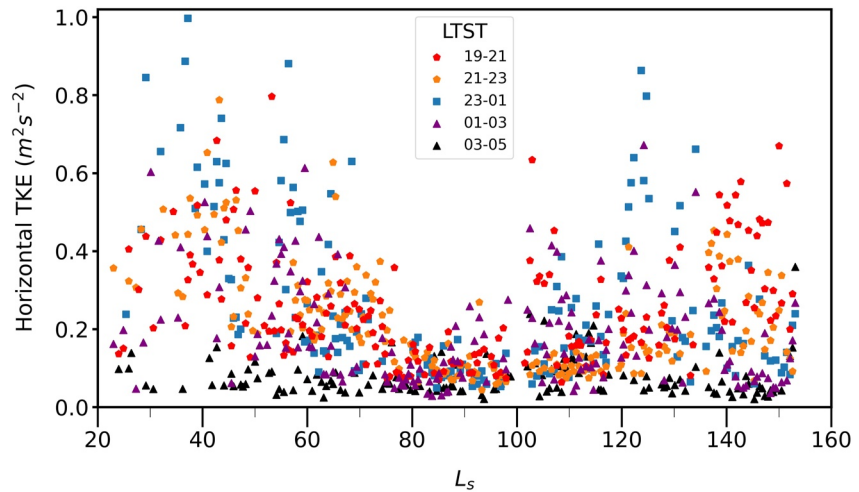


**Figure 5.** MEDA  $TKE_H$  as a function of  $L_s$  averaged for five nighttime observation periods.

### 2.5. Mars Climate Database (MCD) Global Scale Model

The Mars Climate Database (MCD, Forget et al., 1999; Lewis et al., 1999; Millour et al., 2022) is used in Section 3.6 to provide large-scale context to aid in the interpretation of the observations. Note that the spatial resolution of the MCD is  $\sim 5.625 \times 3.75^\circ$  in longitude  $\times$  latitude, therefore Jezero crater is not resolved; data at the Jezero location are interpolated from the coarse MCD grid.

## 3. Results

We show the results of MEDA  $TKE_H$  in Section 3.1, MRAMS TKE in Section 3.2, and the correlation between MEDA  $TKE_H$  and MEDA temperature oscillations in Section 3.3. Then, we show results of the MEDA bulk Richardson number and MRAMS Richardson number in Section 3.4, MRAMS vertical profiles of wind magnitude, wind shear and Richardson number (Ri) in Section 3.5 and contributions of large-scale circulation to Jezero crater turbulence using MCD in Section 3.6.

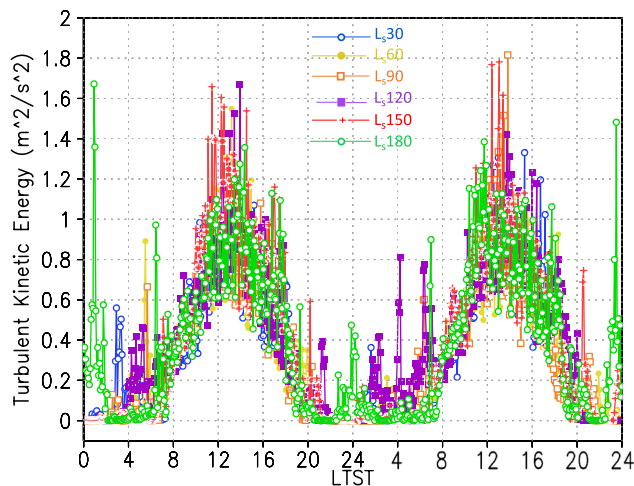
### 3.1. MEDA Horizontal Turbulent Kinetic Energy

Figure 5 shows MEDA  $TKE_H$  at 1.5 m height as a function of  $L_s$  for five nighttime observation periods (19:00–21:00, 21:00–23:00, 23:00–01:00, 01:00–03:00, and 03:00–05:00 LTST). The  $TKE_H$  is calculated every 5 min (Section 2.2, Equation 1) and then averaged over the five nighttime intervals, resulting in one data point for every 2 hours (and five per sol in total).

Figure 5 shows evident turbulence from 19:00 to 03:00 LTST, with stronger turbulence for the 23:00–01:00 LTST period. After 03:00, MEDA  $TKE_H$  values remain low during the whole data set with the exception of sol  $\sim 311$  ( $L_s \sim 152^\circ$ ). Over all earlier times of night shown, there is a high turbulence period from sol  $\sim 50$  ( $L_s \sim 30^\circ$ ) to sols  $\sim 133$  ( $L_s \sim 68^\circ$ ) with two peaks at around sol  $\sim 65$  ( $L_s \sim 37^\circ$ ) and sol  $\sim 107$  ( $L_s \sim 56^\circ$ ), and another high turbulence period during the summer starting at sol  $\sim 211$  ( $L_s \sim 103^\circ$ ) peaking around sol  $\sim 253$  ( $L_s \sim 123^\circ$ ). Between these seasonal turbulence periods, there is a clear hiatus in turbulence centered prior to summer solstice at sol  $\sim 167$  (at  $L_s \sim 83^\circ$ ) and lasting tens of sols.

### 3.2. MRAMS Turbulent Kinetic Energy

The effect of subgrid-scale eddies is captured within MRAMS via a prognostic TKE equation (Mellor & Yamada, 1974) in Figure 6. In MRAMS, TKE



**Figure 6.** Two sols time series of Turbulent Kinetic Energy predicted with Mars Regional Atmospheric Modeling System (MRAMS) for Mars 2020 landing site for  $L_s$  30°, 60°, 90°, 120°, 150°, and 180°.



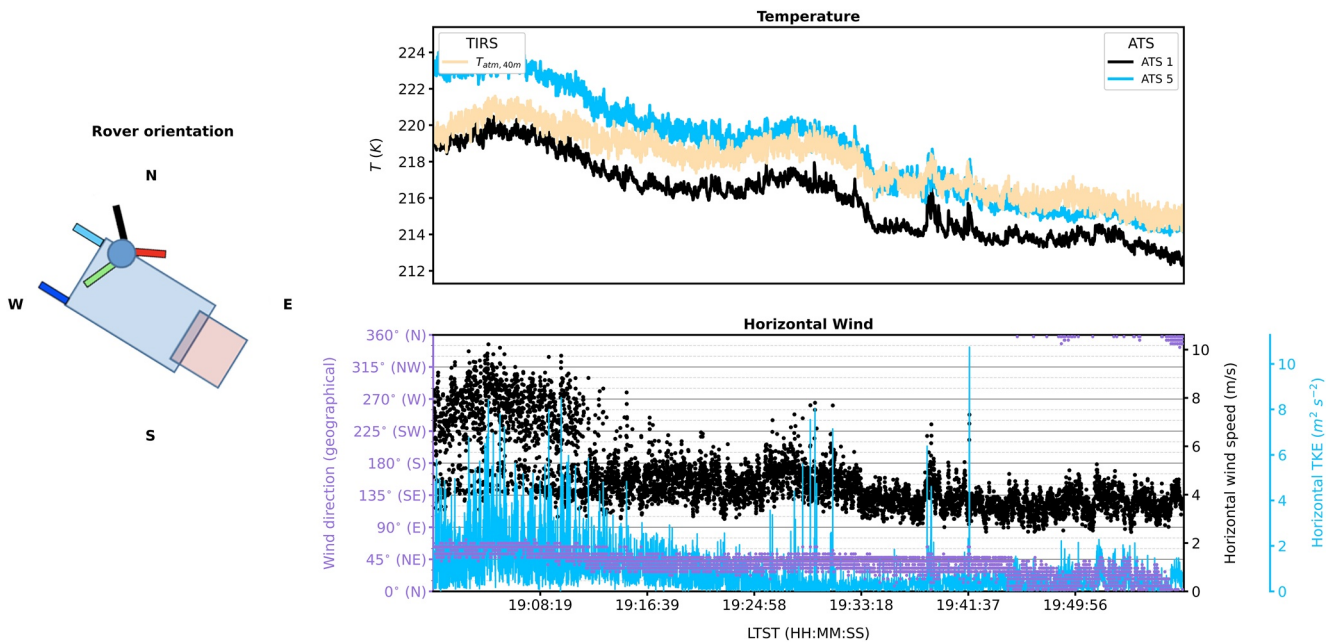


Figure 7. Same as Figure 2 but for sol 85 ( $L_s$  45°) from 19:00 to 20:00.

is the total turbulent kinetic energy that includes contributions from each of the 3D wind components (Mellor & Yamada, 1974). It may be interpreted as the energy contained in the dominant energy-carrying eddies that are too small to be resolved by the model. Although we expect the partitioning of TKE to favor  $TKE_H$  during nighttime stable conditions, TKE could include some contribution from vertical motion, so caution must be exercised when directly comparing MEDA  $TKE_H$  with MRAMS TKE.

The model often shows increases in TKE during the night (Figure 6), especially at  $L_s \sim 30^\circ$ ,  $L_s \sim 120^\circ$  and  $180^\circ$ , and with weak TKE values at  $L_s \sim 60^\circ$  and  $90^\circ$ . Also, there is weak turbulence at  $L_s \sim 150^\circ$  during most of the night except at  $\sim 20:00$  LTST. MEDA  $TKE_H$  (Figure 5) also shows a clear hiatus in turbulence around  $L_s \sim 83^\circ$  and strong values in the period 19:00–21:00 LTST at  $L_s \sim 150^\circ$ . Although the stronger turbulence period is around midnight (23:00–1:00 LTST) in MEDA  $TKE_H$  (Figure 5) for  $L_s \sim 30^\circ$ ,  $\sim 60^\circ$ , and  $\sim 120^\circ$ , there is only development of midnight local turbulence in MRAMS TKE, but with an amplitude as intense as its daytime counterpart, at  $L_s \sim 180^\circ$ . Unfortunately, MEDA wind data during that epoch are unavailable. The model often predicts increases in TKE at the same times as modeled rapid thermal perturbations (Figure 3, blue arrows). Some examples include  $L_s \sim 30^\circ$  at  $\sim 03:00$  LTST;  $L_s \sim 60^\circ$  at  $\sim 21:30$  LTST;  $L_s \sim 120^\circ$  at  $\sim 21:00$  LTST; and  $L_s \sim 180^\circ$  at  $\sim 23:30$  LTST.

### 3.3. Correlation Between MEDA $TKE_H$ and MEDA Temperature Oscillations

Following the procedure explained in Section 2.2, we are able to identify nighttime turbulent events with MEDA that bring warm air masses. Figure 7 and Figures S1–S6 in Supporting Information S1 indicate a strong correlation between temperature oscillations of low and high frequency and the peaks in the  $TKE_H$  which we use as a proxy for near-surface turbulence at Jezero crater. Two peaks in the low frequency temperature oscillations can be seen at around  $\sim 19:06$  and  $\sim 19:30$  LTST, while two events of higher frequency are observed around  $\sim 19:38$  and  $\sim 19:41$  LTST (Figure 7). All these temperature oscillations are consistently observed at the three atmospheric height levels studied (0.84, 1.45, and 40 m), indicating that turbulent events are captured by ATS and TIRS.

As temperatures and  $TKE_H$  vary on different timescales, we analyzed their linear correlation by smoothing the high frequency variations of the  $TKE_H$ . We did this by retaining the maximum values in windows of 10 measurements and then applying a one-dimensional interpolation between those maximums to equalize the time series length of temperature and  $TKE_H$ . By following this strategy, we found that between 19:00 and 20:00 LTST on sol 85, the correlation coefficient between the temperature measurements of ATS1 (Figure 7, top) and the  $TKE_H$  (Figure 7, bottom) was 0.71. This indicates that the temperature and  $TKE_H$  measurements are positively correlated and account for 71% of the peaks in the data. Furthermore, the coefficient of determination,  $R^2$ , is 0.5,

suggesting that 50% of the temperature variations are explained by  $TKE_H$  variations. Therefore, we can conclude that there is a significant correlation between temperatures and  $TKE_H$  as measured by MEDA, even though they vary on different time scales.

A strong dependence of nocturnal turbulence on the ambient wind was also observed at InSight's location (Chatain et al., 2021). Turbulent fluctuations in temperature in Jezero crater are explored further in other manuscripts in this issue: using measurements from ATS (de la Torre-Juarez et al., 2023; Munguira et al., 2023) and the SuperCam microphone (Chide et al., 2022). More examples of the simultaneous fluctuations of air temperature (at 0.85 m, 1.45 and  $\sim 40$  m height) and  $TKE_H$  (at 1.5 m height) as observed by MEDA are shown in the Supporting Information S1 (Figures S1–S6).

### 3.4. Richardson Number

The Richardson number ( $Ri$ ) is a dimensionless parameter that represents the ratio of the buoyancy (indicated by Brunt–Väisälä frequency) to wind shear.

$$Ri = \frac{N^2}{\left(\frac{\partial V}{\partial z}\right)^2}, \quad (2)$$

where  $N$  is the Brunt–Väisälä frequency and  $V$  is the horizontal wind speed. The Richardson number may be used to determine why turbulence occurs, that is, whether it is buoyancy or shear driven. Negative  $Ri$  values point to a buoyancy source of turbulence during unstable conditions for daytime convective periods, while positive  $Ri$  values indicate a buoyancy sink inhibiting turbulence in nighttime stable conditions (Stull, 1988). However, an initially laminar flow, for example, in a typical strongly stable nighttime condition on Mars may become turbulent for  $0 < Ri < 0.25$ . At this point, the wind-shear source of turbulence dominates the buoyancy sink producing nighttime turbulence, either because the wind shear is strong and/or because the stability is weak (Chatain et al., 2021).

$Ri$  provides insight into the observed fluctuations of MEDA  $TKE_H$  during nighttime, as demonstrated in Figure 8, where a comparison between the MRAMS  $Ri$  and a proxy of the bulk  $Ri$  calculated using MEDA data (MEDA  $R_B$ ) is shown. These variations can be attributed to seasonal changes, and  $Ri$  can aid in the interpretation of these fluctuations. Care must be taken in comparing these two numbers, however. MRAMS  $Ri$  is calculated from Equation 2 using the two lowest model atmospheric levels at  $\sim 14.5$  and  $\sim 46.5$  m. On the other hand, MEDA  $R_B$  is derived using the ground temperature as a proxy for the first atmospheric layer and the air temperature at  $\sim 1.5$  m as the second atmospheric layer. Therefore, MEDA  $R_B$  assumes that the ground temperature is identical to the lowest atmospheric temperature and is valid over the very lowest layers of the atmosphere, as described in more detail in Martínez et al. (2023):

$$\text{MEDA } R_B = \frac{g}{T_g} \frac{(T_a - T_g)z_a}{U_a^2}, \quad (3)$$

where  $g$  is gravitational acceleration,  $T_a$  is the air temperature at  $\sim 1.45$  m,  $T_g$  is the surface brightness temperature,  $U_a$  is the horizontal wind speed at  $\sim 1.5$  m measured by the MEDA WS and  $z_a = 1.45$  is the height of the MEDA ATS. Equation 3 assumes that the ground temperature ( $T_g$ ) is representative of the very low atmospheric temperature. In contrast, MRAMS uses atmospheric temperatures that are valid within model layers and the resulting  $Ri$  is valid over the deeper atmospheric layer. Even though there is a disparity in the computation of  $Ri$  between MEDA and MRAMS, the values can be qualitatively compared by looking for differences between seasons. The regimes implied by certain values of  $Ri$  are “no turbulence” for  $Ri$  values  $> 1$ , “stably stratified weak turbulence” for  $0.25 < Ri < 1$ , “forced shear-driven turbulence” for  $0 < Ri < 0.25$  and “buoyancy-driven turbulence” for negative  $Ri$  values.

Looking at Figure 8, it is clear that this region of Jezero crater is susceptible to turbulence during the night, with Richardson number values below 0.25 during several periods of all the seasons considered, corresponding to a shear-driven turbulent regime. As expected, the Richardson number values remain negative (buoyancy-driven turbulence) during the daytime in all seasons shown here.

Based on Martínez et al. (2023) (Section 4.2.3), the unexpected nighttime-negative MEDA  $R_B$  values could be produced by the presence of an unstable convective layer instead of a thermal inversion. This unexpected scenario

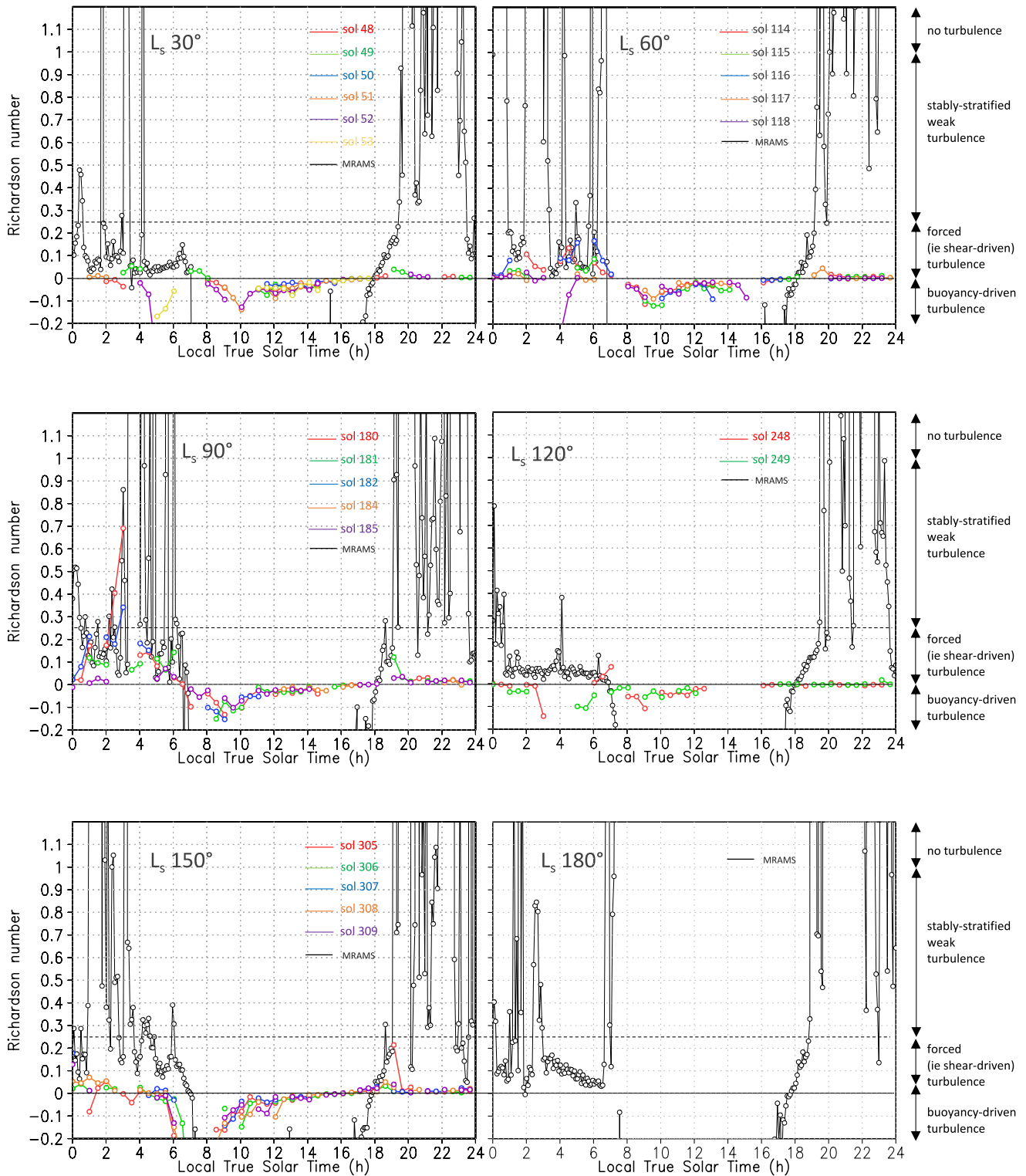


**Figure 8.** Mars Regional Atmospheric Modeling System (MRAMS) Richardson number (MRAMS  $R_i$ ) at the Mars 2020 landing site for  $L_s$   $30^\circ$ ,  $60^\circ$ ,  $90^\circ$ ,  $120^\circ$ ,  $150^\circ$ , and  $180^\circ$  (black dots) and a proxy of the MEDA bulk Richardson number (MEDA  $R_B$ ) diurnal time series over the corresponding sols available (colored dots). Also indicated to the right is the regime implied by different values of Richardson number.

mostly occurred on sols with localized terrains with thermal inertia (TI) values higher than the mean values across Perseverance's traverse obtained from MEDA (TI > 350 SI units). The reason for the apparent disappearance of nighttime inversions is that surface temperatures are controlled (in large part) by very local surface properties, whereas local air temperatures are controlled by not only exchange with the local surface but also transport and mixing over a much larger area. In other words, on these sols, we expect that a nighttime inversion still existed on average over the larger area, but the surface within the TIRS IR5 FOV was warmer than the average surface temperature due to a higher TI very locally. Hence, the surface temperature used in the MEDA  $R_B$  Equation 3 for those sols may not be appropriate either.

Generally, based on MRAMS  $Ri$  values, the atmosphere at Jezero close to the surface is slightly stable and susceptible to shear-driven turbulence during the first part of the night (~19:00–19:30 LTST) and around midnight, with increasing susceptibility to shear-driven turbulence in the last hours of the night. Around sunset, the collapse of the martian PBL is very dramatic (Banfield et al., 2020) and at Jezero crater it typically starts around ~17:00–17:30 LTST (Munguira et al., 2023) when there is a clear, strong and quick transition from a susceptible to buoyancy-driven turbulence atmosphere to a susceptible to forced (shear-driven) turbulence atmosphere in MRAMS  $Ri$  for all the seasons.

At  $L_s \sim 30^\circ$  the environment is conducive to turbulence at around 19:00–19:30, 23:30–00:30 LTST and then from 01:00 LTST until sunrise (very strong after 04:00 LTST). However, from 01:00 to 04:00 LTST, there are short periods lasting 5–15 min during which MRAMS  $Ri$  values are very large, so nighttime turbulence is likely to be suppressed or absent. Because  $N^2 > 0$  at night, we conclude that any turbulence will be mechanically forced.  $L_s \sim 30^\circ$  has lower MRAMS  $Ri$  and MEDA  $R_B$  values when compared to  $L_s \sim 60^\circ$ , when there is reduced MRAMS  $Ri$  between 01:00 and 02:00 LTST and between 03:30 LTST and sunrise with short periods during which nighttime turbulence is likely to be suppressed.

It is clear that  $L_s \sim 90^\circ$  is the least favorable season for nocturnal turbulence, in agreement with MEDA  $TKE_H$  (Figure 5), with the highest nocturnal MEDA  $R_B$  values of all the data set (above 0.25 at sols 180 and 182) and with only occasional low MRAMS  $Ri$  between ~23:30 and 03:00 LTST and in some periods between 04:00 LTST and sunrise, but there are also periods where it is  $\gg 0.25$ .

At  $L_s \sim 120^\circ$ , the atmosphere is very susceptible to nocturnal turbulence, in agreement with MEDA  $TKE_H$  (Figure 5), with persistent low MRAMS  $Ri$  values from ~00:45 LTST to dawn and low MEDA  $R_B$  values during the night, with the special caveat that we had limited MEDA observations during that period (only sols 248 and 249) due to a mission flight software update.

At  $L_s \sim 150^\circ$  there is a persistent reduction in MRAMS  $Ri$  values between ~22:45 and 23:45 LTST, from midnight to ~01:00 LTST, around ~03:00 and ~04:00 LTST, and between 04:30 LTST and dawn. Due to the mentioned WS failure at  $L_s \sim 152^\circ$ , there are no MEDA  $R_B$  values at  $L_s \sim 180^\circ$ , but there are persistent low MRAMS  $Ri$  values between ~00:15 and ~01:15 LTST, from ~01:50 to ~02:20 LTST and moreover between ~03:00 LTST and dawn. Very strong (MRAMS  $Ri = 0$ ) at 02:00 LTST.

Once the critical Richardson Number is reached ( $Ri \lesssim 0.25$ ), shear instabilities can mix warmer air aloft down to the surface (Banfield et al., 2020; Miles, 1961; Spiga & Forget, 2009). This turbulent mixing process has been observed in the Owens Valley (USA) under similar katabatic wind conditions emanating from the Sierra Mountains (Whiteman, 1982; Whiteman & Doran, 1993). MEDA air temperature data show periodic pulses of warm air at night, as a result of atmospheric turbulence and are not caused by rover perturbations. These nighttime turbulent events bring warm air masses, observed at the three atmospheric height levels, as determined through correlations between peaks in the MEDA  $TKE_H$  and MEDA temperature fluctuations, as shown in Figure 7 and Figures S1–S6 in Supporting Information S1.

### 3.5. MRAMS Vertical Profiles

MRAMS vertical profiles from the surface up to ~1 km high of wind magnitude, wind shear, and Richardson number ( $Ri$ ) at the Mars 2020 landing site for  $L_s$  30°, 60°, 90°, 120°, 150°, and 180° are shown in Figure 9. All values are averaged over the five-time ranges shown: 19:00–21:00, 21:00–23:00, 23:00–01:00, 01:00–03:00, and 03:00–05:00 LTST.  $Ri$  is out of range in Figure 9 for most of the altitude range, as we have limited the range to  $-0.25$  to  $1.25$  in order to search for nighttime environments conducive to turbulence. On Earth, the presence of a strong shear below an LLJ can significantly impact the turbulent exchange between the surface and the atmosphere (Baas et al., 2009; Banta

et al., 2006; Conangla & Cuxart, 2006). Wind tunnel experiments have demonstrated that the shear generated by an LLJ can result in intermittent bursts of turbulence in the lower section of the stable boundary layer (Ohya et al., 2008). Looking at wind magnitudes of Figure 9, the generated shear is primarily observed some hundreds of meters above the surface, but always below ~800 m height; therefore,  $Ri$  values are shown as solid lines below that height and as dotted lines above that level because there is no certainty that the latter will affect the flow at the surface.

A description of the MRAMS nighttime atmospheric susceptibility to turbulence shown in Figure 9 is given below, separated into the six different times of year studied:

- At  $L_s \sim 30^\circ$  there is moderate atmospheric susceptibility to nighttime stably stratified weak turbulence close to the surface increasing from 23:00 to 05:00 LTST. Wind shear near the surface is strongest late in the night at that time before sunrise and is important during the first part of the night from 19:00 to 23:00 LTST. The susceptibility to atmospheric turbulence in this period of the year, although moderate, is stronger than at  $L_s \sim 60^\circ$  and moreover  $\sim 90^\circ$ .
- At  $L_s \sim 60^\circ$  there is susceptibility to nighttime stably stratified weak turbulence during the first part of the night, around 19:00–21:00 LTST and also before sunrise, between 03:00 and 05:00 LTST, compared to the rest of the night. The wind shear near the surface is strongest before sunrise, between 03:00 and 05:00 LTST, important between 19:00–21:00 LTST and very low between 21:00–23:00 LTST. Although the wind shear is also strong between 01:00 and 03:00 LTST, the higher Brunt–Väisälä frequency value compared to 03:00 and 05:00 LTST periods leads to high  $Ri$  values, that is, with no susceptibility to turbulence.
- $L_s 90^\circ$  has the most unfavorable conditions for turbulence, with the highest  $Ri$  values throughout the night near the surface. There are some favorable conditions conducive to turbulence between 01:00–03:00 LTST, but some hundreds of meters above the surface.
- $L_s \sim 120^\circ$  has the highest atmospheric susceptibility to nighttime turbulence of all the times of year studied, with  $Ri \lesssim 0.25$  (forced turbulence) near the surface produced by a very strong wind shear after midnight and before sunrise (01:00–05:00 LTST), and with moderate  $Ri$  values (stably stratified weak turbulence) and strong wind shear from 23:00 to 01:00 LTST.
- At  $L_s \sim 150^\circ$ , the most interesting period of the night is around midnight, between 23:00 and 01:00, when strong turbulence near the surface could be produced by a strong wind shear. There are also some favorable conditions for turbulence in the first moments of the night, 19:00–21:00 LTST, but some hundreds of meters above the surface.
- $L_s \sim 180^\circ$  has a high atmospheric susceptibility to nighttime wind shear-driven turbulence, but this is contained exclusively to the period before sunrise, that is, from 03:00 to 05:00, when strong wind shear is produced close to the surface. There are also some favorable conditions for turbulence in the first moments of the night (19:00–21:00 LTST) but some hundreds of meters above the surface.

The strongest wind shear near the surface in Figure 9 almost always occurs in the period before sunrise, between 03:00 and 05:00 LTST, followed by the period 01:00–03:00 LTST (especially for  $L_s \sim 30^\circ$ ,  $\sim 120^\circ$ , and  $\sim 180^\circ$ ), although the strongest wind shear near the surface at  $L_s \sim 150^\circ$  occurs between 23:00 and 01:00 LTST. The strong wind shear near the surface is related to the presence of strong near surface winds of ~10–17 m/s peaking at ~46.5 m. The clear near-surface stable inversions inhibit vertical mixing; hence, wind shear is the only source of turbulence.

The origin of this nocturnal turbulence is explored using cross sections of the MRAMS model output. Figures 10–12 show vertical slices from west to east across Jezero crater at Mars 2020 latitude (18.44°N) at 20:00 (Figure 10), 00:00 (Figure 11) and 04:00 LTST (Figure 12), and from 18:00 to 07:00 LTST in the animations included in the Supporting Information S1 as a function of all the six times of the year, from MRAMS grid #7.

Jezero crater is embedded inside and close to the NW rim of the Isidis basin, whose daytime regional upslope (~east-southeasterly) and nighttime regional downslope (~northwesterly) surface winds dominate (Newman et al., 2021; Pla-García et al., 2020). Animations (Supporting Information S1) and Figures 10–12 show nighttime downslope surface flow developing from the west rim of Jezero crater and undercutting the regional easterly (westward) strong LLJ aloft during the first part of the night (~19:00–01:00 LTST). Looking at wind magnitudes in Figure 9 (left panels), the strongest LLJ is always found at 19:00–21:00 LTST (black line). In Figures 10 and 11 there is a very strong wind shear produced by the moderate NW downslope winds undercutting the strong LLJ of about ~24 m/s at 20:00 LTST (Figure 10, all  $L_s$ ) and ~16 m/s at 00:00 LTST (Figure 11, bottom right  $L_s \sim 180^\circ$ ) with LLJ peaking at about ~1–2 km height and producing instabilities that mix air aloft down to the surface and producing the turbulence observed by the rover between 19:00 and 01:00 LTST. As time goes on

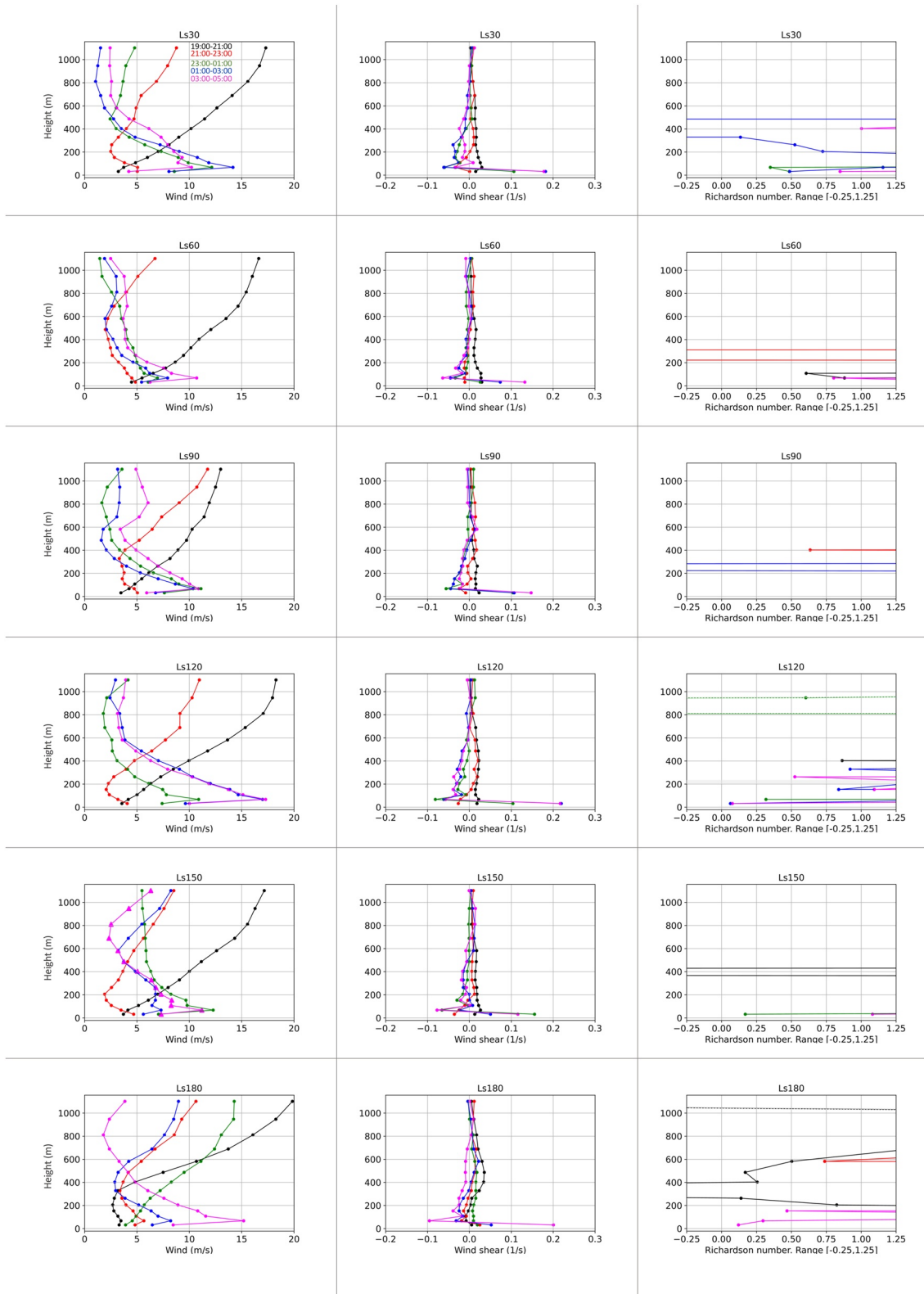


**Figure 9.** Mars Regional Atmospheric Modeling System (MRAMS) vertical profiles of wind magnitude, wind shear and Richardson number at the Mars 2020 landing site for  $L_s$  30°, 60°, 90°, 120°, 150°, and 180°.

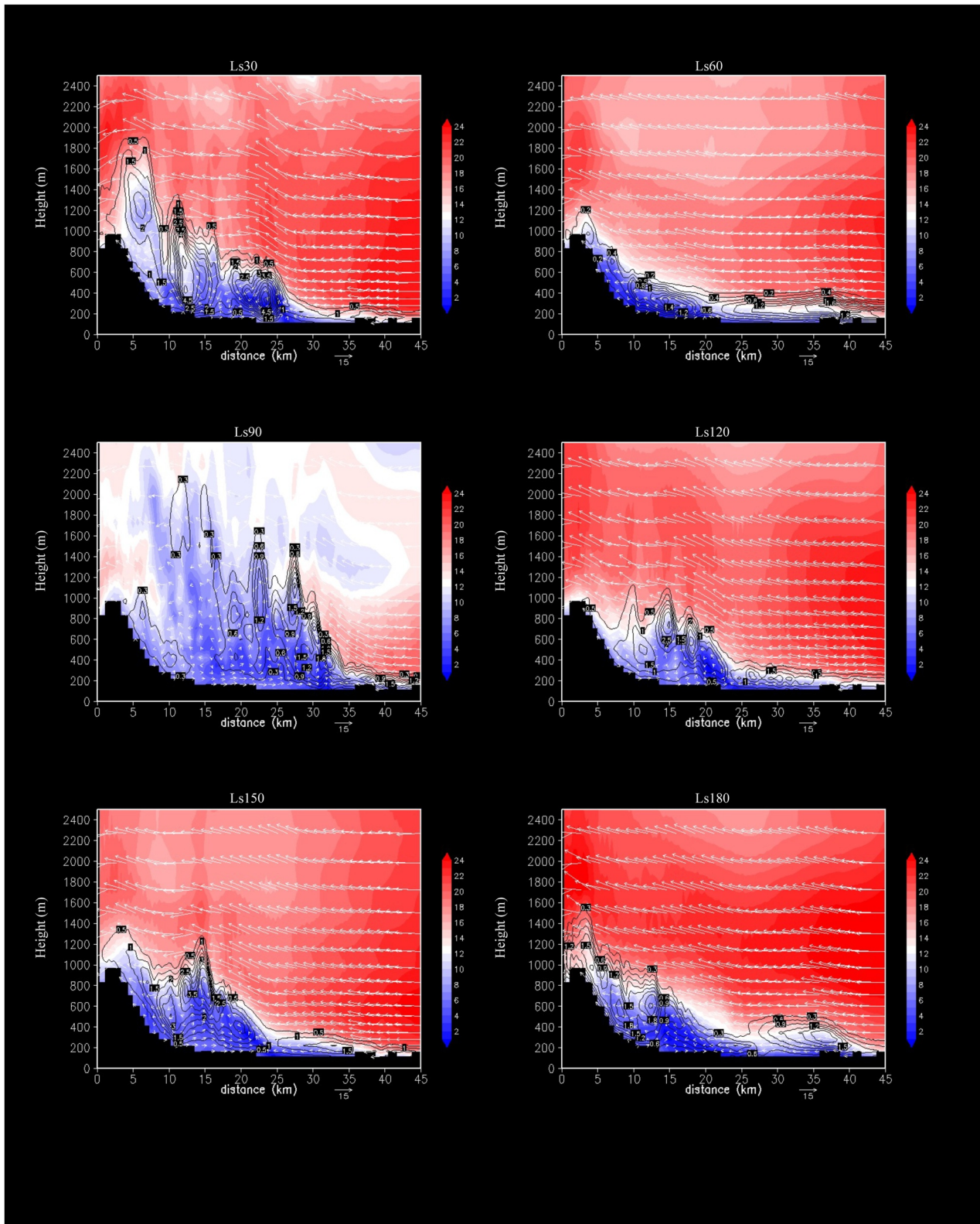


**Figure 10.** Mars Regional Atmospheric Modeling System (MRAMS) model cross-section of winds at 20:00 LTST of  $L_s$  30°, 60°, 90°, 120°, 150°, and 180°. Jezero's west rim is on the left and the east rim on the right. The total horizontal wind in colored shadows. Winds are also shown with white arrows in which the vertical component has increased  $\times 5$ . Values of TKE are shown in black contours. The Perseverance rover landing site location corresponds to  $x = 17.5$ .

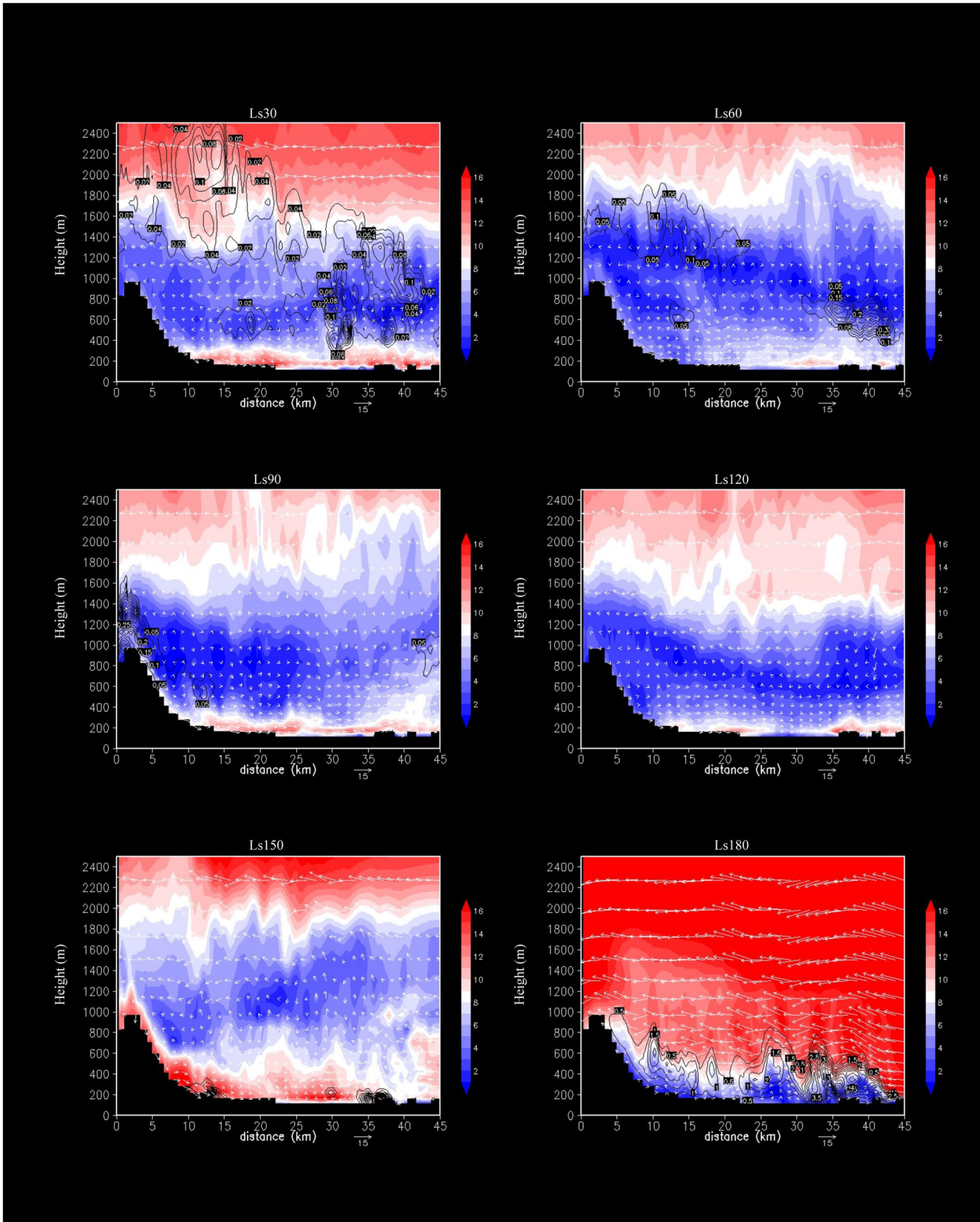


Figure 11. Same as Figure 10 but for 00:00 LTST.



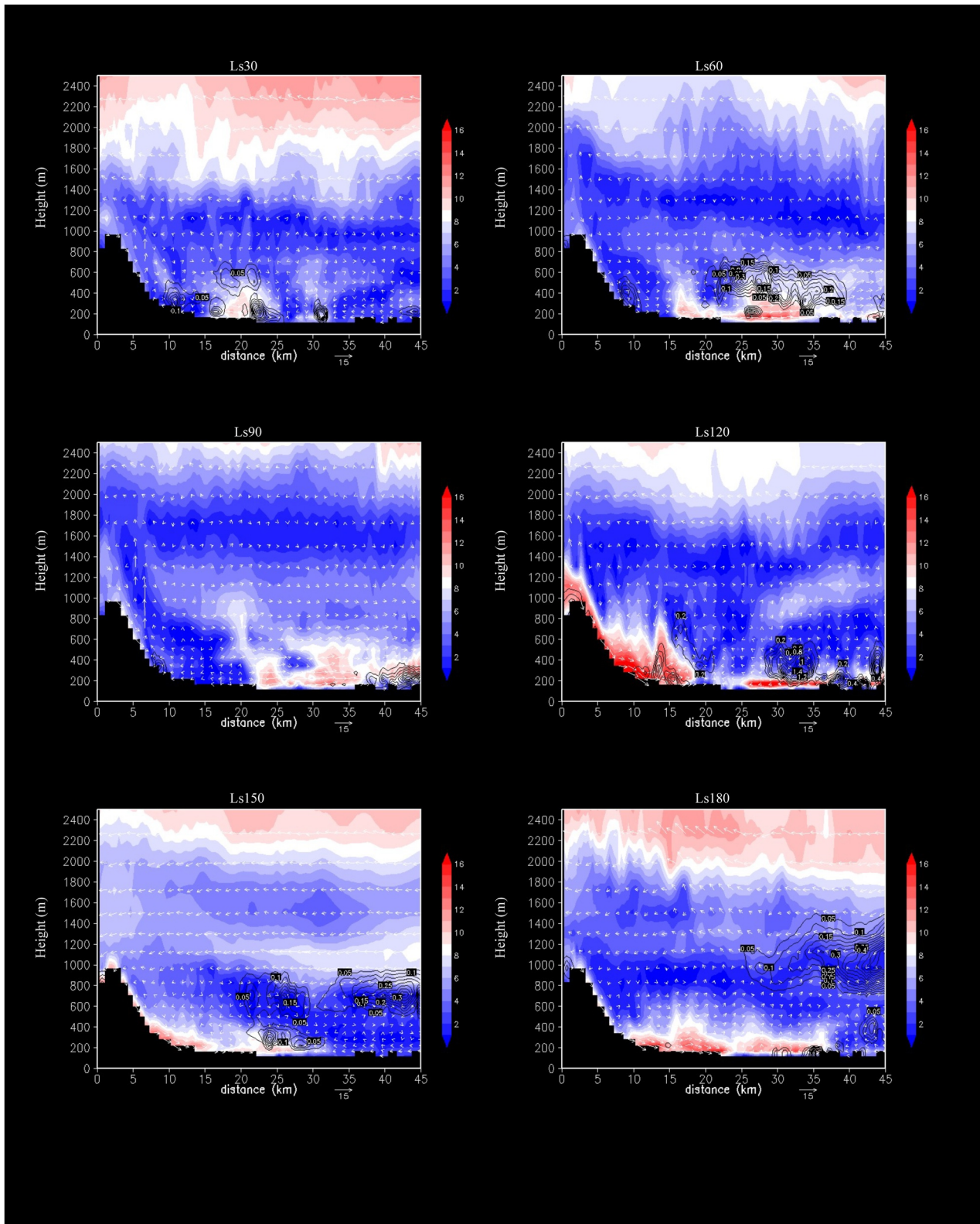


Figure 12. Same as Figure 10 but for 04:00 LTST.

through the night, the magnitude of the LLJ decreases (left panels of Figures 9–12) as it does the observed turbulence computed in MEDA  $TKE_H$  in Figure 5.

For many of the periods of the year, the local downslope front at the surface from the west rim appears to take the form of an atmospheric bore wave (Figures 10–12). Atmospheric bore waves have been suspected to exist on Mars based on imagery (Banfield et al., 2020; Hunt et al., 1981; Kahn & Gierasch, 1982; Pickersgill, 1984) and modeling (Sta. Maria et al., 2006). A key environmental factor allowing atmospheric bore propagation is the presence of a LLJ directed opposite to the movement of the atmospheric bore with significant turbulence developed in the layer between the LLJ maximum and the surface (Haghi & Durran, 2021), as shown in Figures 10 and 11, but a bore could also form without the presence of a LLJ if the downslope surface winds developing from the west rim are strong enough and undercut weak winds aloft during the last part of the night (Figure 12,  $L_s \sim 120^\circ$ ). During these hours (03:00–05:00 LTST), there is a strong wind-shear in the model (Figures 9 and 12) leading to mechanical turbulence that is not observed in the MEDA data set, where we have low wind speeds (Figure 4) and low MEDA  $TKE_H$  values (Figure 5). An explanation for this disagreement could be that the MRAMS model gives the general trend of how atmosphere dynamics behave at Jezero crater, given the initial state. The model does appear to be doing a remarkably good job in reproducing a LLJ and surface winds and is consistent with previous modeling; however, the observations always remain complex to interpret because they correspond to one point on the map with a very local dynamic around the rover, and we can see that it is difficult to compare with the model results. The measurements indicate some trends and the modeling is consistent with part of the observations, but these observations are probably not sufficient to conclude about atmosphere dynamics at Jezero crater.

Based on the model results, the turbulence observed in Jezero crater is likely caused by the passage of an atmospheric bore wave related to shallow westerly (eastward) downslope winds from the west rim. During the first part of the night ( $\sim 19:00$ – $01:00$  LTST), wind shear turbulence is produced when those moderate downslope winds undercut a very strong easterly (westward) LLJ aloft, while during the second part of the night ( $\sim 01:00$  LTST–dawn), the LLJ clearly weakens, strengthening the eastward downslope winds that undercut weak winds aloft, producing the wind shear turbulence. In both periods, the downslope front propagates from the crater rim toward the interior basin, like an atmospheric bore wave. The enhancing wind shear leads to a reduction in the  $Ri$  and the onset of mechanical turbulence; that is essentially why atmospheric bores produce turbulence in their wake. As mentioned, once the critical Richardson Number is reached ( $Ri \lesssim 0.25$ ), shear instabilities can mix warmer air aloft down to the surface, something noticeable when looking at the MRAMS TKE values of Figures 10–12, where we see the turbulence packages being transported from aloft to the surface. The five-minute output of the model shows the propagation of the atmospheric bore wave as it moves from west to east (from left to right in Figures 10–12 and animations) downslope through the west rim first and then toward the east through the domain at a propagation speed of  $\sim 10$ – $15$  m s $^{-1}$ . The observed typical propagation speed for the bore waves was 6.8–27.6 m s $^{-1}$  at Tharsis region (Pickersgill, 1984) and 17–22 m s $^{-1}$  at Elysium Planitia (Banfield et al., 2020) and the propagation speed for the modeled bore waves predicted in Sta. Maria et al. (2006) was 17–20 m s $^{-1}$ . These propagation speeds compare relatively well to those predicted by the MRAMS model in this study. To gain additional appreciation for the complexity and beauty of atmospheric bore wave propagation within Jezero Crater, the reader should proceed no further without first viewing the animations of the circulations provided in the Supporting Information S1. This atmospheric bore mechanism differs from the breaking mountain waves suggested as nighttime turbulence driver at Gale crater (Rafkin et al., 2016). The evidence of significant mountain wave activity in Jezero crater during the entire period studied with MRAMS is lower compared to Gale crater.

### 3.6. Contributions of the Large-Scale Wind to Jezero Crater Turbulence

Figure 13 shows the zonal winds as predicted by the MCD at the location of Jezero crater between 1 and 4 km height. A nighttime regional easterly (westward) LLJ is present between  $\sim 19:00$  and  $\sim 01:00$  LTST, in agreement with Figures 9–12. This jet corresponds to a planetary-scale circulation feature forced by the diurnal cycle and the large-scale collapse of the PBL, whose mixing is parameterized in the MCD (Colaitis et al., 2013). This large-scale feature significantly contributes to the overall wind field above Jezero crater, although the latter remains dominated by the local scale circulation. The low-level (peaking at  $\sim 1$ – $2$  km) zonal winds above Jezero crater first reverse at sunset (they are eastward during the day, then westward during the night) and then intensifies during the nighttime. This change in wind direction and the subsequent nighttime intensification of the LLJ may be the result of different factors. First, the region is adjacent to Syrtis Major (Figure 1), a large-scale  $\sim 1,000$  km $^2$  region with (a) a low surface albedo, which causes surface temperatures to be warmer than the surrounding terrains, yielding enhanced infrared radiative heating of the near-surface atmosphere, and (b) high-elevation terrains. Both effects

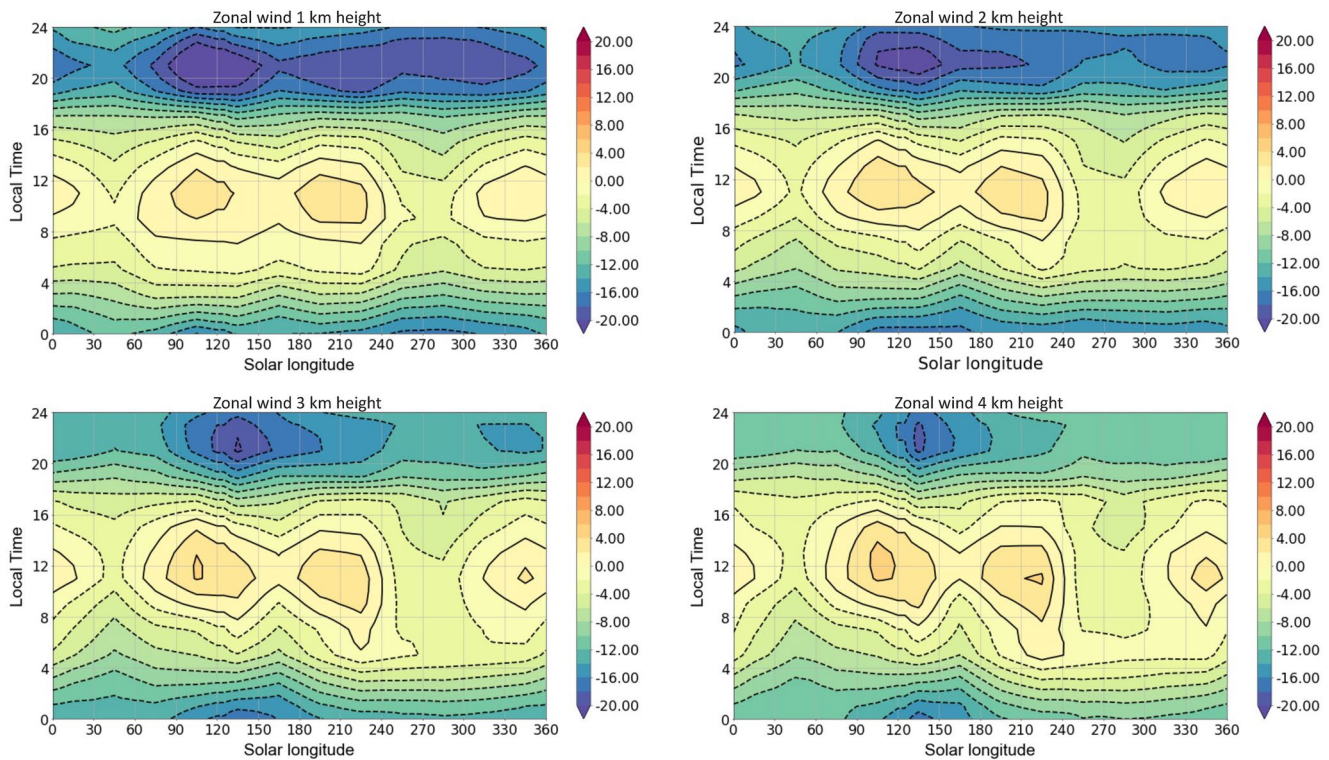


**Figure 13.** The diurnal cycle of horizontal eastward (+; solid contour lines) and westward (-; dashed contour lines) winds at Mars 2020 location as obtained using the Mars Climate Database (MCD) for 1, 2, 3, and 4 km height over an entire year.

should lead to a more vigorous PBL during the daytime in this region (see Figure 16 in Colaitis et al., 2013). The MCD predicts a large 10 km maximal PBL height in the afternoon in the vicinity of Syrtis Major, which is roughly 30% larger than what is predicted in the surrounding regions. The large-scale collapse of the PBL in this region therefore leads to intense pressure changes with longitude and intense changes in vertical mixing during the PBL collapse, favoring changes in wind direction and the formation of a strong low-level jet in the Jezero crater region during the nighttime. Other factors could combine and contribute such as the large-scale circulation and global tide effects Hinson and Wilson (2004). Figure 13 shows that a stronger westward LLJ is produced at all seasons during the first part of the night (~19:00–01:00 LTST) and dramatically weakens from ~01:00 LTST until dawn, in agreement with our MRAMS results, which show similar patterns in Figures 9–12.

#### 4. Summary and Conclusions

Nighttime observations of rapid horizontal wind and air temperature fluctuations by MEDA sensors show the development of nocturnal local turbulence in Jezero crater. As derived both from observations and modeling, nocturnal turbulence at the rover's location in Jezero crater peaks at  $L_s \sim 30^\circ\text{--}60^\circ$  and at  $L_s \sim 120^\circ\text{--}180^\circ$ , but is weakest between those periods at around  $L_s \sim 90^\circ$  (northern summer solstice). Interesting periods of high nocturnal turbulence occur at 19:00–21:00 LTST and around midnight. The large-scale circulation may set the conditions for the formation of a strong low-level jet in the Jezero crater region during the nighttime, but it is not sufficient to explain the turbulence that is observed locally at Jezero crater.

MRAMS results are in good agreement with MEDA observations, and this agreement provides justification for utilizing the model results to investigate the origin of the nocturnal turbulence environment of the Jezero crater region and the mechanisms at play. Our modeling results provide evidence that points toward the observed nighttime turbulence being caused by the passage of atmospheric bore waves inside Jezero crater. Those atmospheric bores would be produced during the first part of the night (~19:00–01:00 LTST) by shallow westerly (eastward) downslope winds developing from the west rim of Jezero crater when undercut a strong easterly (westward) low-level jet aloft, that peaks about ~1–2 km in height. Subsequently, during the second part of the night (from

~01:00 LTST until dawn), the LLJ noticeably weakens, causing the eastward downslope winds to strengthen and undercut weaker winds aloft, thereby generating wind shear turbulence. In both time periods, the downslope front propagates from the west crater rim toward the interior basin, resembling the behavior of an atmospheric bore wave and producing enhanced wind shear, with or without the presence of a LLJ, leading to a reduction in the  $Ri$  and an onset of mechanical turbulence. Once the critical Richardson Number is reached ( $Ri \sim <0.25$ ), shear instabilities can mix warmer air aloft down to the surface. Looking at MEDA data, we are able to identify nighttime turbulent events that bring warm air masses, observed at the three atmospheric height levels, when a strong correlation is present between temperature oscillations and peaks in the MEDA  $TKE_H$ .

Atmospheric bores differ from the breaking mountain waves suggested as nighttime turbulence driver at Gale crater (Rafkin et al., 2016). The evidence of significant mountain wave activity in Jezero crater during the entire period studied with MRAMS is lower compared to Gale crater.

The SuperCam microphone has also observed significant temperature fluctuations that are attributable to atmospheric turbulence (Maurice et al., 2022; Mimoun et al., 2023). During the period analyzed in this paper ( $L_s$  13°–180°), the microphone was mostly operated during the daytime; however, with only a handful of nighttime recordings, coincident recordings of nocturnal turbulence were not made. Murdoch et al. (2022) and Stott et al. (2023) found a definitive recording of nocturnal turbulence on sol 454 ( $L_s \sim 237^\circ$ ) just after midnight (~00:21 LTST) attributed to wind (Stott et al., 2023, Figure 2e), inside our studied period 23:00–01:00 where we observed the greatest nocturnal turbulence (Figure 5 and Figures S5 and S6 in Supporting Information S1). Combining the sampling rate of MEDA with the high sampling rate of the microphone, the suite of sensors on Perseverance will enable the characterization of nocturnal turbulence at a wider range of scales than ever before.

Our results demonstrate that the continuous high-frequency atmospheric measurements by Mars 2020 MEDA sensors are key to unveiling the properties of Martian nighttime turbulence and provide valuable data for testing and refining the physics involved, as encapsulated within atmospheric models. Similarly, models of the atmospheric circulation in Jezero crater are valuable for interpreting these data.

## Data Availability Statement

All Mars 2020 MEDA data necessary to reproduce each figure shown in this manuscript are available via the Planetary Data System (PDS) Atmospheres node as the Mars Environmental Dynamics Analyzer (MEDA) Experiment Data Record (EDR) and Reduced Data Record (RDR) Data Products Archive Bundle (de la Torre Juárez & Rodríguez-Manfredi, 2021). The MRAMS mesoscale model data set, animations and tools for Jezero crater nighttime turbulence analysis are provided for the periods studied in this manuscript in Pla-García and Rafkin (2023).

## References

- Baas, P., Bosveld, F. C., Klein Baltink, H., & Holtslag, A. A. M. (2009). A climatology of nocturnal low-level jets at Cabauw. *Journal of Applied Meteorology and Climatology*, 48(8), 1627–1642. <https://doi.org/10.1175/2009jamc1965.1>
- Banfield, D., Spiga, A., Newman, C., Forget, F., Lemmon, M., Lorenz, R., et al. (2020). The atmosphere of Mars as observed by InSight. *Nature Geoscience*, 13(3), 190–198. <https://doi.org/10.1038/s41561-020-0534-0>
- Banta, R. M., Pichugina, Y. L., & Brewer, W. A. (2006). Turbulent velocity-variance profiles in the stable boundary layer generated by a nocturnal low-level jet. *Journal of the Atmospheric Sciences*, 63(11), 2700–2719. <https://doi.org/10.1175/jas3776.1>
- Chatain, A., Spiga, A., Banfield, D., Forget, F., & Murdoch, N. (2021). Seasonal variability of the daytime and nighttime atmospheric turbulence experienced by InSight on Mars. *Geophysical Research Letters*, 48(22), e2021GL095453. <https://doi.org/10.1029/2021gl095453>
- Chide, B., Bertrand, T., Lorenz, R. D., Munguira, A., Hueso, R., Sánchez-Lavega, A., et al. (2022). Acoustics reveals short-term air temperature fluctuations near Mars' surface. *Geophysical Research Letters*, 49(21), e2022GL100333. <https://doi.org/10.1029/2022gl100333>
- Colaitis, A., Spiga, A., Hourdin, F., Rio, C., Forget, F., & Millour, E. (2013). A thermal plume model for the Martian convective boundary layer. *Journal of Geophysical Research: Planets*, 118(7), 1468–1487. <https://doi.org/10.1002/jgre.20104>
- Conangla, L., & Cuxart, J. (2006). On the turbulence in the upper part of the low-level jet: An experimental and numerical study. *Boundary-Layer Meteorology*, 118(2), 379–400. <https://doi.org/10.1007/s10546-005-0608-y>
- Davis, P. A. (2000). Development and mechanisms of the nocturnal jet. *Meteorological Applications*, 7(3), 239–246. <https://doi.org/10.1017/s1350482700001535>
- Davy, R., Davis, J. A., Taylor, P. A., Lange, C. F., Weng, W., Whiteway, J., & Gunnlaugson, H. P. (2010). Initial analysis of air temperature and related data from the phoenix met station and their use in estimating turbulent heat fluxes. *Journal of Geophysical Research*, 115(E3), E00E13. <https://doi.org/10.1029/2009je003444>
- de la Torre Juárez, M., Chavez, A., Tamppari, L. K., Munguira, A., Martínez, G., Hueso, R., et al. (2023). Diurnal cycle of air temperature fluctuations at Jezero crater. *Journal of Geophysical Research*. <https://doi.org/10.1029/2022JE007458>
- de la Torre Juárez, M., & Rodríguez-Manfredi, J. A. (2021). Mars 2020 MEDA Bundle. *NASA Planetary Data System*. <https://doi.org/10.17189/1522849>

## Acknowledgments

This research was funded by Grant RTI2018-098728-B-C31 and PN2021-PID2021-126719OB-C41 by the Spanish Ministry of Science and Innovation/State Agency of Research MCIN/AEI/10.13039/501100011033. AM, ASL, TR, and RH were supported by Grant PID2019-109467GB-I00 funded by MCIN/AEI/10.13039/501100011033 and by Grupos Gobierno Vasco IT1366-19. Part of this research was carried out at the Jet Propulsion Laboratory, California Institute of Technology, under a contract with the National Aeronautics and Space Administration (80NM0018D0004). The JPL co-authors acknowledge funding from NASA's Space Technology Mission Directorate and the Science Mission Directorate. CEN was supported by funding from the Mars 2020 mission, part of the NASA Mars Exploration Program.

- Forget, F., Hourdin, F., Fournier, R., Hourdin, C., Talagrand, O., Collins, M., et al. (1999). Improved general circulation models of the Martian atmosphere from the surface to above 80 km. *Journal of Geophysical Research*, *104*(E10), 24155–24175. <https://doi.org/10.1029/1999je001025>
- Haghi, K. R., & Durran, D. R. (2021). On the dynamics of atmospheric bores. *Journal of the Atmospheric Sciences*, *78*(1), 313–327. <https://doi.org/10.1175/jas-d-20-0181.1>
- Hinson, D. P., & Wilson, R. J. (2004). Temperature inversions, thermal tides, and water ice clouds in the Martian tropics. *Journal of Geophysical Research*, *109*(E1), E01002. <https://doi.org/10.1029/2003je002129>
- Hueso, R., Newman, C. E., Río-Gaztelurrutia, T. D., Munguira, A., Sánchez-Lavega, A., Toledo, D., et al. (2022). Convective vortices and dust devils detected and characterized by Mars 2020. *Journal of Geophysical Research: Planets*, *128*, e2022JE007516. <https://doi.org/10.1029/2022JE007516>
- Hunt, G. E., Pickersgill, A. O., James, P. B., & Evans, N. (1981). Daily and seasonal Viking observations of Martian bore wave systems. *Nature*, *293*(5834), 630–633. <https://doi.org/10.1038/293630a0>
- Joshi, M. M., Haberle, R. M., Barnes, J. R., Murphy, J. R., & Schaeffer, J. (1997). Low-level jets in the NASA Ames Mars general circulation model. *Journal of Geophysical Research*, *102*(E3), 6511–6523. <https://doi.org/10.1029/96JE03765>
- Kahn, R., & Gierasch, P. (1982). Long cloud observations on Mars and implications for boundary layer characteristics over slopes. *Journal of Geophysical Research*, *87*(A2), 867–880. <https://doi.org/10.1029/ja087ia02p00867>
- Lewis, S. R., Collins, M., Read, P. L., Forget, F., Hourdin, F., Fournier, R., et al. (1999). A climate database for Mars. *Journal of Geophysical Research*, *104*(E10), 24177–24194. <https://doi.org/10.1029/1999je001024>
- Lorenz, R. D., & Setzen, K. S. (2014). Buoyant thermal plumes from planetary landers and rovers: Application to sizing of meteorological masts. *Planetary and Space Science*, *90*, 81–89. <https://doi.org/10.1016/j.pss.2013.10.011>
- Martínez, G. M., Sebastián, E., Vicente-Retortillo, A., Smith, M. D., Johnson, J. R., Fischer, E., et al. (2023). Surface energy budget, Albedo, and thermal inertia at Jezero Crater, Mars, as observed from the Mars 2020 MEDA instrument. *Journal of Geophysical Research: Planets*, *128*(2), e2022JE007537. <https://doi.org/10.1029/2022je007537>
- Maurice, S., Chide, B., Murdoch, N., Lorenz, R. D., Mimoun, D., Wiens, R. C., et al. (2022). In situ recording of Mars soundscape. *Nature*, *605*(7911), 653–658. <https://doi.org/10.1038/s41586-022-04679-0>
- Mellor, G., & Yamada, T. (1974). A hierarchy of turbulence closure models for planetary boundary layers. *Journal of the Atmospheric Sciences*, *31*(7), 1791–1806. [https://doi.org/10.1175/1520-0469\(1974\)031<1791:ahotcm>2.0.co;2](https://doi.org/10.1175/1520-0469(1974)031<1791:ahotcm>2.0.co;2)
- Miles, J. W. (1961). On the stability of heterogeneous shear flows. *Journal of Fluid Mechanics*, *10*(4), 496–508. <https://doi.org/10.1017/s0022112061000305>
- Millour, E., Forget, F., Spiga, A., Pierron, T., Bierjon, A., Montabone, L., et al. (2022). The Mars climate database, version 6.1. In *Seventh international workshop on the Mars atmosphere. Modelling and Observations*.
- Mimoun, D., Cadu, A., Murdoch, N., Chide, B., Sournac, A., Parot, Y., et al. (2023). The Mars microphone onboard SuperCam. *Space Science Reviews*, *219*(1), 5. <https://doi.org/10.1007/s11214-022-00945-9>
- Munguira, A., Hueso, R., Sánchez-Lavega, A., de la Torre-Juarez, M., Martínez, G. M., Newman, C. E., et al. (2023). Near surface atmospheric temperatures at Jezero from Mars 2020 MEDA measurements. *Journal of Geophysical Research: Planets*, *128*(3), e2022JE007559. <https://doi.org/10.1029/2022je007559>
- Murdoch, N., Stott, A. E., Gillier, M., Hueso, R., Lemmon, M., Martínez, G., et al. (2022). The sound of a Martian dust devil. *Nature Communications*, *13*(1), 7505. <https://doi.org/10.1038/s41467-022-35100-z>
- Newman, C. E., De La Torre Juarez, M., Pla-García, J., Wilson, R. J., Lewis, S. R., Neary, L., et al. (2021). Multi-model meteorological and Aeolian predictions for Mars 2020 and the Jezero Crater region. *Space Science Reviews*, *217*(1), 1–68.
- Newman, C. E., Hueso, R., Lemmon, M. T., Munguira, A., Vicente-Retortillo, Á., Apestigue, V., et al. (2022). The dynamic atmospheric and Aeolian environment of Jezero crater, Mars. *Science Advances*, *8*(21), eabn3783. <https://doi.org/10.1126/sciadv.abn3783>
- Ohya, Y., Nakamura, R., & Uchida, T. (2008). Intermittent bursting of turbulence in a stable boundary layer with low-level jet. *Boundary-Layer Meteorology*, *126*(3), 349–363. <https://doi.org/10.1007/s10546-007-9245-y>
- Oke, T. R. (1987). *Boundary layer climates*. Methuen.
- Perez-Grande, I., Peinado, L., Chamorro, A., Torralbo, I., Alonso, G., Rodríguez Manfredi, J. A., et al. (2017). Thermal design of the air temperature sensor (ATS) and the Thermal InfraRed Sensor (TIRS) of the Mars environmental dynamics analyzer (MEDA) for Mars 2020. In *47th international conference on environmental systems*.
- Pérez-Izquierdo, J., Sebastián, E., Martínez, G. M., Bravo, A., Ramos, M., & Manfredi, J. A. R. (2018). The Thermal Infrared Sensor (TIRS) of the Mars environmental dynamics analyzer (MEDA) instrument onboard Mars 2020, a general description and performance analysis. *Measurement*, *122*, 432–442. <https://doi.org/10.1016/j.measurement.2017.12.004>
- Pickersgill, A. O. (1984). Martian bore waves of the Tharsis region: A comparison with Australian atmospheric waves of elevation. *Journal of the Atmospheric Sciences*, *41*(8), 1461–1473. [https://doi.org/10.1175/1520-0469\(1984\)041<1461:mbwott>2.0.co;2](https://doi.org/10.1175/1520-0469(1984)041<1461:mbwott>2.0.co;2)
- Pla-García, J., Rafkin, S. C., Karatekin, Ö., & Goesener, E. (2019). Comparing MSL Curiosity rover TLS-SAM methane measurements with Mars Regional Atmospheric Modeling System atmospheric transport experiments. *Journal of Geophysical Research: Planets*, *124*(8), 2141–2167. <https://doi.org/10.1029/2018je005824>
- Pla-García, J., & Rafkin, S. C. R. (2023). MRAMS mesoscale model dataset, animations and tools for Jezero crater nighttime turbulence analysis [Dataset]. Zenodo. <https://doi.org/10.5281/zenodo.7829838>
- Pla-García, J., Rafkin, S. C. R., Kahre, M., Gomez-Elvira, J., Hamilton, V. E., Navarro, S., et al. (2016). The meteorology of Gale crater as determined from rover environmental monitoring station observations and numerical modeling. Part I: Comparison of model simulations with observations. *Icarus*, *280*, 103–113. <https://doi.org/10.1016/j.icarus.2016.03.013>
- Pla-García, J., Rafkin, S. C. R., Martínez, G. M., Vicente-Retortillo, Á., Newman, C. E., Savijärvi, H., et al. (2020). Meteorological predictions for Mars 2020 Perseverance Rover landing site at Jezero crater. *Space Science Reviews*, *216*(8), 1–21. <https://doi.org/10.1007/s11214-020-00763-x>
- Rafkin, S. C. R. (2009). A positive radiative-dynamic feedback mechanism for the maintenance and growth of Martian dust storms. *Journal of Geophysical Research*, *114*(E1), E01009. <https://doi.org/10.1029/2008je003217>
- Rafkin, S. C. R., Haberle, R. M., & Michaels, T. I. (2001). The Mars regional atmospheric modeling System (MRAMS): Model description and selected simulations. *Icarus*, *151*(2), 228–256. <https://doi.org/10.1006/icar.2001.6605>
- Rafkin, S. C. R., & Michaels, T. (2019). The Mars regional atmospheric modeling System (MRAMS): Current status and future directions. *Atmosphere*, *10*(12), 747. <https://doi.org/10.3390/atmos10120747>
- Rafkin, S. C. R., Pla-García, J., Kahre, M., Gomez-Elvira, J., Hamilton, V. E., Marín, M., et al. (2016). The meteorology of Gale crater as determined from rover environmental monitoring station observations and numerical modeling. Part II: Interpretation. *Icarus*, *280*, 114–138. <https://doi.org/10.1016/j.icarus.2016.01.031>

- Rafkin, S. C. R., Sta Maria, M. R. V., & Michaels, T. I. (2002). Simulation of the atmospheric thermal circulation of a mar-tian volcano using a mesoscale numerical model. *Nature*, *419*(6908), 697–699. <https://doi.org/10.1038/nature01114>
- Read, P. L., Galperin, B., Larsen, S. E., Lewis, S. R., Määttä, A., Petrosyan, A., et al. (2017). The Martian planetary boundary layer. In R. M. Haberle, R. T. Clancy, F. Forget, M. D. Smith, & R. W. Zurek (Eds.), *The atmosphere and climate of Mars (Cambridge planetary science)* (pp. 172–202). Cambridge University Press. <https://doi.org/10.1017/9781139060172.007>
- Rodriguez-Manfredi, J. A., De la Torre Juárez, M., Alonso, A., Apéstigue, V., Arruego, I., Atienza, T., et al. (2021). The Mars Environmental Dynamics Analyzer, MEDA. A suite of environmental sensors for the Mars 2020 mission. *Space Science Reviews*, *217*(3), 1–86.
- Schofield, J. T., Barnes, J. R., Crisp, D., Haberle, R. M., Larsen, S., Magalhães, J. A., et al. (1997). The Mars pathfinder atmospheric structure investigation/meteorology (ASI/MET) experiment. *Science*, *278*(5344), 1752–1758. <https://doi.org/10.1126/science.278.5344.1752>
- Sebastián, E., Martínez, G. M., Ramos, M., Haenschke, F., Ferrándiz, R., Fernández, M., & Manfredi, J. A. R. (2020). Radiometric and angular calibration tests for the MEDA-TIRS radiometer onboard NASA's Mars 2020 mission. *Measurement*, *164*, 107968. <https://doi.org/10.1016/j.measurement.2020.107968>
- Sebastián, E., Martínez, G. M., Ramos, M., Perez-Grande, I., Sobrado, J., & Manfredi, J. A. R. (2021). Thermal calibration of the MEDA-TIRS radiometer onboard NASA's perseverance rover. *Acta Astronautica*, *182*, 144–159. <https://doi.org/10.1016/j.actaastro.2021.02.006>
- Smith, M. D., Wolff, M. J., Lemmon, M. T., Spanovich, N., Banfield, D., Budney, C. J., et al. (2004). First atmospheric science results from the Mars exploration rovers mini-TES. *Science*, *306*(5702), 1750–1753. <https://doi.org/10.1126/science.1104257>
- Smith, M. D., Wolff, M. J., Spanovich, N., Ghosh, A., Banfield, D., Christensen, P. R., et al. (2006). One Martian year of atmospheric observations using MER Mini-TES. *Journal of Geophysical Research*, *111*(E12), E12S13. <https://doi.org/10.1029/2006JE002770>
- Spiga, A., & Forget, F. (2009). A new model to simulate the Martian mesoscale and microscale atmospheric circulation: Validation and first results. *Journal of Geophysical Research*, *114*(E2), E02009. <https://doi.org/10.1029/2008je003242>
- Sta Maria, M., Rafkin, S. C., & Michaels, T. I. (2006). Numerical simulation of atmospheric bore waves on Mars. *Icarus*, *185*(2), 383–394. <https://doi.org/10.1016/j.icarus.2006.07.006>
- Stott, A. E., Murdoch, N., Gillier, M., Banfield, D., Bertrand, T., Chide, B., et al. (2023). Wind and turbulence observations with the Mars microphone on Perseverance. *Journal of Geophysical Research*, *128*, e2022JE007547. <https://doi.org/10.1002/essoar.10512263.1>
- Stull, R. (1988). *An introduction to boundary layer meteorology*. Kluwer Academic Publishers.
- Thorpe, A. J., & Guymmer, T. H. (1977). The nocturnal jet. *Quarterly Journal of the Royal Meteorological Society*, *103*(438), 633–653. <https://doi.org/10.1002/qj.49710343809>
- Viúdez-Moreiras, D., Lemmon, M., Newman, C. E., Guzewich, S., Mischna, M., Gómez-Elvira, J., et al. (2022). Winds at the Mars 2020 landing site: 1. Near-surface wind patterns at Jezero Crater. *Journal of Geophysical Research: Planets*, *127*(12), e2022JE007522. <https://doi.org/10.1029/2022je007522>
- Whiteman, C. D. (1982). Breakup of temperature inversions in deep mountain valleys: Part I. Observations. *Journal of Applied Meteorology and Climatology*, *21*(3), 270–289. [https://doi.org/10.1175/1520-0450\(1982\)021<0270:botiid>2.0.co;2](https://doi.org/10.1175/1520-0450(1982)021<0270:botiid>2.0.co;2)
- Whiteman, C. D., & Doran, J. C. (1993). The relationship between overlying synoptic-scale flows and winds within a valley. *Journal of Applied Meteorology and Climatology*, *32*(11), 1669–1682. [https://doi.org/10.1175/1520-0450\(1993\)032<1669:trboss>2.0.co;2](https://doi.org/10.1175/1520-0450(1993)032<1669:trboss>2.0.co;2)